Cloudy bag model for the S-D wave $\bar{K}$-N system

Guangliang He and Rubin H. Landau
Physics Department, Oregon State University, Corvallis, Oregon 97331
(Received 2 August 1993)

The cloudy quark bag model is applied to the coupled ($\bar{K}N$, $\Sigma\pi$, $\Lambda\pi$) system for S-D partial waves. Energy-dependent separable potentials are derived, as are new numerical algorithms for solving the coupled Lippmann-Schwinger equations. The parameters of the model are fit to K^-p scattering and reaction cross sections, branching ratios, and mass spectra from $K^-p \to \Sigma\pi\pi\pi, \Lambda\pi\pi\pi$. Within the constraints of the model, the branching ratio and $\Sigma\pi$ mass spectrum data are in conflict. The $\Sigma_{P13}(1385)$ and $\Lambda_{D03}(1520)$ resonances are found to be predominately elementary bag states with considerable dressing for the Σ_{P13}. The $\Lambda_{S01}(1405)$ appears as a complicated composite systems arising from two poles. The model with certain parameter sets does predict two sign changes in the real part of the $\bar{K}N$ scattering amplitude near threshold, but they are not quite at the correct energies to produce agreement with the sign of the strong interaction shift of kaonic hydrogen.

PACS number(s): 14.20.Jn, 12.40.Aa, 13.75.Jz

I. INTRODUCTION

It is generally accepted that hadrons are composed of quarks and that strong interactions among quarks will be explained by quantum chromodynamics (QCD). Unfortunately, QCD is still too complicated to solve and so we construct phenomenological models which incorporate confinement, asymptotic freedom, and the symmetries of QCD—yet still permit analysis of experimental data and application to nuclear few-body systems. The MIT "bag" [1] is a model for a bubble in the QCD vacuum and imposes confinement by placing the quarks in a finite bag of about 1 fm radius. If the model were interpreted literally, this large a bag would shatter conventional nuclear physics since nuclei would be filled more with quarks than nucleons.

Soon after its introduction it was realized that the bag model violates chiral symmetry (conservation of quark helicity)—the second best symmetry ($\sim 7\%$) of the strong interactions [2]. The violation arises from quark reflections off the bag wall changing the quark's momentum but not its spin. The symmetry is restored by coupling in a pion field to the bag's surface [3–5]. In the "little brown bag" of Brown and Rho [4], an interior phase contains free, massless quarks, while an exterior phase contains pions but no quarks. The pressure of the pion field on the outside of the bag then compresses the bag down to the very small 0.3 fm little brown bag. Clearly with this small a bag there will be very few quark effects expected inside of nuclei, and the conventional views of nuclei as collections of nucleons exchanging mesons holds.

In the cloudy bag model (CBM) of Miller, Thomas, and collaborators [6–13], the exterior pion field gets quantized and penetrates the bag. While the CBM's Lagrangian is nonlinear, practical calculations are carried out as a perturbation expansion with the zeroth order term yielding the MIT bag model. The first tests of the CBM dealt with static properties of hadrons, such as charge radii and magnetic moments, and were successful [12,13]. Later tests dealt with dynamic properties, such as pion-nucleon scattering, and required an extension of the Lagrangian to incorporate volume in addition to surface coupling [10]. Since the extension incorporated Weinberg's effective πN Lagrangian, it is not surprising that success was found [14,15].

In order to study the KN and $\overline{K}N$ systems, strangeness was incorporated into the CBM by extending the Lagrangian from SU(2) to SU(3) [16,17]. However, the complications of thresholds and exotic KN resonances led Veit *et al.* [18] to conclude that the model "has trouble with resonances" for both the $\overline{K}N$ and KN systems. For example, they found a $\overline{K}N$ scattering amplitude which appeared to have a Λ resonance signal approximately 5 MeV below threshold rather than the expected 27 MeV below. Further analysis by Fink *et al.* [19] indicated that the resonance signal arises from the influence of the threshold cusp on a pole some 13 MeV *above* threshold.

The $\bar{K}N$ findings are interesting because they reflect on the nature of the subthreshold Λ resonance and possibly on the puzzling experimental measurements of the $1S$ strong interaction level shift in kaonic hydrogen [20–22]. The hydrogen experiments indicate that the real part of the K^-p scattering amplitude has either no or two sign changes right above threshold [19,23–25], whereas K matrix analyses and most potential models predict one sign change. The CBM fits have two sign changes close to threshold, but on either side of threshold.

It has not been clear to us what level of agreement to expect between models of the $\bar{K}N$ coupled system and energy-dependent scattering and reaction data. On the one hand the CBM assumption of a rigid spherical bag and of pointlike pion fields is possibly too simple, yet on the other hand it may be that only more partial waves are needed to get the energy dependence right. There is, after all, experimental indication that significant P-wave scattering enters at 184 MeV/c [26], and there is the D-wave resonance at 390 MeV/c. To describe additional data and to test the model further, we have ex-

tended the $\bar{K}N$ cloudy bag model to include the P and D partial waves. This extends the contact interaction to include spacelike terms in addition to timelike ones, and the general interaction to include spin-orbit forces. We have deduced effective potentials for use in a Lippmann-Schwinger equation, and have fit the potentials' parameters to data up to 520 MeV/c. We were aided in our work by the similar kaon work of Veit *et al.* [17]—similar, yet with the additional and stronger interactions available to the antikaon making for more differences than similarities.

II. CLOUDY BAG LAGRANGIAN

The MIT bag model's Lagrangian is [3,5]

$$\mathcal{L}_{\rm MIT}(x) = \left(\frac{i}{2}\bar{q}\overleftrightarrow{\not\partial}q - B\right)\theta_v - \frac{1}{2}\bar{q}q\,\delta_s. \tag{1}$$

Here q is the quark field, B is a universal constant called the "bag pressure," and for a nondeformable, static, spherical bag, the bag ansatz is imposed by setting the volume step function $\theta_v = \theta(R-r)$ and the surface delta function $\delta_s = \delta(R-r)$. By demanding that the action $S = \int d^4x\,\mathcal{L}(x)$ remains stationary under arbitrary changes in q, $\bar{q}$, θ_v, and δ_s, we obtain the equations of motion

$$i\,\not\partial q(x) = 0 \qquad (r < R), \tag{2}$$

$$i\,\not n q(x) = q(x) \quad (r = R), \tag{3}$$

$$B = -\frac{1}{2}n\cdot\partial\left[\bar{q}(x)q(x)\right]_{r=R}. \tag{4}$$

For the static case, the unit normal to the bag's surface is $n^\mu = (0,\hat{\mathbf{r}})$. Equation (2) is the Dirac equation inside the bag, (3) is the linear boundary condition of confinement, and (4) is the stability condition on the bag pressure. We shall use solutions to these equations in constructing the baryon-meson effective potentials.

The Lagrangian (1) does not preserve chiral symmetry since the surface term $\frac{1}{2}\bar{q}q\delta_s$ reverses the helicity of the quark hitting the bag's surface. To incorporate chiral symmetry, a pion field $\vec{\phi}$ is coupled throughout the bag's volume [3–5]:

$$\mathcal{L}_{\rm CBM} = \left(\frac{i}{2}\bar{q}\overleftrightarrow{\not\partial}q - B\right)\theta_v - \frac{1}{2}\bar{q}e^{i\vec{\tau}\cdot\vec{\phi}\gamma_5/f}q\delta_s + \frac{1}{2}\left(D_\mu\vec{\phi}\right)^2. \tag{5}$$

Here the arrow over $\vec{\phi}$ indicates its isovector nature, $\vec{\tau}$ is a vector of Pauli matrices for SU(2) (isospin), f is the meson octet decay constant, and D_μ is the covariant derivative:

$$D_\mu\vec{\phi} = (\partial_\mu\phi)\hat{\phi} + f\sin(\phi/f)\partial_\mu\hat{\phi}, \tag{6}$$

$$\phi = \left(\vec{\phi}\cdot\vec{\phi}\right)^{1/2}, \quad \hat{\phi} = \vec{\phi}/\phi. \tag{7}$$

While the Lagrangian (5) has no obvious predictions for low-energy pion-nucleon scattering, Thomas [10] transformed it to one containing a volume coupling of the covariant derivative of the quark field:

$$\mathcal{L}_{\rm CBM} = \left(\frac{i}{2}\bar{q}\overleftrightarrow{\not D}q - B\right)\theta_v - \frac{1}{2}\bar{q}q\delta_s + \frac{1}{2}\left(D_\mu\vec{\phi}\right)^2 + \frac{1}{2f}\bar{q}\gamma^\mu\gamma_5\vec{\tau}q\cdot(D_\mu\vec{\phi})\theta_v, \tag{8}$$

$$D_\mu q = \partial_\mu q - i\left[\frac{\cos(\phi/f)-1}{2}\right]\vec{\tau}\cdot\left(\hat{\phi}\times\partial_\mu\hat{\phi}\right)q. \tag{9}$$

This Lagrangian incorporates the Weinberg-Tomozawa relation for zero-energy S-wave pion scattering.

III. APPLICATION TO $\bar{K}N$ SCATTERING

To apply the Lagrangian (8) to $\bar{K}N$ scattering, Veit *et al.* [16–18] extended the internal symmetry from flavor SU(2)×SU(2) to SU(3)×SU(3). The quark field q then becomes any member of the SU(3) triplet (u,d,s), the meson field $\vec{\phi}$ any member of the octet, the SU(2) Pauli matrices $\vec{\tau}$ are replaced by $SU(3)$ Gell-Mann matrices $\vec{\lambda}$, and the cross product in the covariant derivative (9) includes SU(3) structure constants $(\vec{A}\times\vec{B})_c = \sum_{a,b} f_{abc}A_aB_b$. Since $\vec{\phi} = 0$ yields the MIT bag Lagrangian (1), which was successful for static baryon properties, Veit *et al.* [16] postulated that if the energy is low, then small ϕ should be a good approximation for scattering. Accordingly, they expanded $\mathcal{L}_{\rm CBM}$ around $\phi = 0$ to obtain the linearized, volume-coupled, SU(3)×SU(3), CBM Lagrangian

$$\mathcal{L}_{\rm CBM} = \mathcal{L}_{\rm MIT} + \mathcal{L}_M + \mathcal{L}_s + \mathcal{L}_c, \tag{10}$$

$$\mathcal{L}_M = \frac{1}{2}(\partial_\mu\vec{\phi})^2, \tag{11}$$

$$\mathcal{L}_s = \frac{\theta_v}{2f}\bar{q}\,\gamma^\mu\,\gamma_5\,\vec{\lambda}q\cdot(\partial_\mu\vec{\phi}), \tag{12}$$

$$\mathcal{L}_c = -\frac{\theta_v}{(2f)^2}\bar{q}\,\gamma^\mu\,\vec{\lambda}\cdot(\vec{\phi}\times\partial_\mu\vec{\phi})q, \tag{13}$$

where $\mathcal{L}_{\rm MIT}$ (1) describes the free bag, $\mathcal{L}_M$ the free meson field, $\mathcal{L}_s$ the s-channel interaction, and $\mathcal{L}_c$ the contact interaction.

In our application of the CBM to the $\bar{K}N$ system, we restrict the energy to $(1250 \le E_{\rm c.m.} \le 1550)$ MeV, that is, to both sides of the $\bar{K}N$ threshold at 1432 MeV. For these energies we consider the six, strangeness -1, baryon-meson (BM) channels which couple strongly:

$$K^-p \to \begin{cases} K^-p & (\text{"threshold"})\ 1432\ \text{MeV}, \\ \bar{K}^0n & -5\ \text{MeV}, \\ \Sigma^-\pi^+ & +95\ \text{MeV}, \\ \Sigma^0\pi^0 & +104\ \text{MeV}, \\ \Sigma^+\pi^- & +103\ \text{MeV}, \\ \Lambda\pi^0 & +181\ \text{MeV}. \end{cases} \tag{14}$$

This system supports a number of resonances which appear in different channels below and above threshold. For

TABLE I. Channel assignment for charge and isospin bases.

	1	2	3	4	5
Charge basis	K^-p	$\bar{K}^0n$	$\Sigma\pi$ $(I=0)$	$\Sigma\pi$ $(I=1)$	$\Lambda\pi^0$
Isospin basis	$\bar{K}N(I=0)$	$\bar{K}N(I=1)$	$\Sigma\pi$ $(I=0)$	$\Sigma\pi$ $(I=1)$	$\Lambda\pi^0$

low energies the relevant ones are $\Lambda_{LI\,2J=S01}(1405)$ and $\Sigma_{P13}(1385)$ below threshold and $\Lambda_{D03}(1520)$ above.

The calculations to follow get rather complicated and so we have placed many of the details in appendixes. We will describe how we extended the CBM up to D waves and in each partial wave deduced effective potentials to be used in the Lippmann-Schwinger equation

$$T_{\beta\alpha}(\mathbf{k}',\mu';\mathbf{k},\mu) = V_{\beta\alpha}(\mathbf{k}',\mu';\mathbf{k},\mu) + \sum_{\gamma,\nu}\int d^3p\,\frac{V_{\beta\gamma}(\mathbf{k}',\mu';\mathbf{p},\nu)T_{\gamma\alpha}(\mathbf{p},\nu;\mathbf{k},\mu)}{E+i\epsilon-E_\gamma(p)}. \quad (15)$$

Here the incident and final particles are in channels α and β (defined in Table I), have spin μ and μ', and center-of-mass (c.m.) momenta $\mathbf{k}$ and $\mathbf{k}'$. The intermediate state is channel γ with spin ν and with a channel momentum $k_{0\gamma}$ determined by setting the channel energy equal to the system energy E:

$$E_\gamma(k_{0\gamma}) = E, \quad (16)$$

$$E_\gamma(p) = E_1(p)+E_2(p) = \sqrt{m_1^2+p^2}+\sqrt{m_2^2+p^2}, \quad (17)$$

where the subscripts 1 and 2 refer to the specific particles in channel γ.

The solution T of the Lippmann-Schwinger equation (15) automatically includes all iterations (ladder graphs) of the potentials but ignores crossed meson lines—which we assume to be small [11]. The derivation of the potentials $V_{\beta\alpha}$ proceed via several steps. First in Sec. III A we specify the coupled-channels Lippmann-Schwinger equation in the partial wave basis. Next in Sec. III B we convert the Lagrangian (8) and (9) into a Hamiltonian, and separate off pieces which produce interactions. Then we obtain the resonant potentials (Sec. III C) and the contact potentials (Sec. III D) from the Foch-space matrix elements:

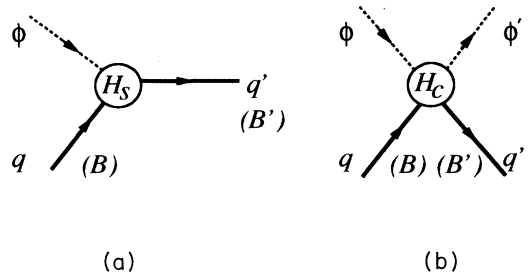

FIG. 1. Feynman diagrams for meson interactions in the cloudy bag model: (a) via the s-channel Hamiltonian H_s, (b) via the contact Hamiltonian H_c. Dashed lines represent mesons and solid lines fermions (quarks or baryons).

$$V_{\beta\alpha} = \langle\beta|H_c|\alpha\rangle + \sum_{B_0=S01,D03,P13}\langle\beta|H_s|B_0\rangle\frac{1}{E-M_{B_0}}\langle B_0|H_s|\alpha\rangle. \quad (18)$$

The first term in (18) describes direct scattering via an elementary quark transition in the contact interaction as illustrated in Fig. 1(b). The B_0 sum in (18) is over the processes, each second order in the H_s Hamiltonian illustrated in Fig. 1(a), in which there are elementary resonance intermediate states as shown in Fig. 2. Resonances with bare masses M_{S01}, M_{P13}, and M_{D03}—but no widths—are thus built into the potential (as opposed to generated by it). However, when the potential gets used as the driving term in the Lippmann-Schwinger equation (15), these elementary resonances get "dressed," that is, the resulting T matrix contains resonances at shifted masses and with finite widths. Furthermore, we treat the elementary masses as adjustable parameters and let the data determine the best values. When the fitting is complete we then have dressed resonance energies and widths as determined from the behavior of the T matrix, as well as best-fit values for the bare masses. As we shall see, there is no guarantee that the bare masses and resonance energies are close. In addition, the potential derived from the contact interaction H_c generates "two-body" or "composite resonances" in T which are not explicit in the potential and thus not elementary.

A. Partial wave Lippmann-Schwinger equation

We assume the standard spin $0\times\frac{1}{2}$ partial wave expansions for the T matrix [27]:

$$T_{\beta\alpha}(\mathbf{k}',\mu';\mathbf{k},\mu) = \frac{1}{2\pi^2}\sum_l\left[(l+1)T^{l+}_{\beta\alpha}(k',k)+lT^{l-}_{\beta\alpha}(k',k)\right]\delta_{\mu'\mu}P_l(x) + \frac{1}{2\pi^2}\sum_l\left[T^{l+}_{\beta\alpha}(k',k)-T^{l-}_{\beta\alpha}(k',k)\right]\langle\mu'|i\boldsymbol{\sigma}\cdot\hat{n}|\mu\rangle P_l'(x), \quad (19)$$

$$T^{lj}_{\beta\alpha}(k',k) = \frac{\pi}{2}\sum_{m,m,\mu\mu'} \langle lm';\tfrac{1}{2}\mu'|l\tfrac{1}{2};jM\rangle\langle lm;\tfrac{1}{2}\mu|l\tfrac{1}{2};jM\rangle \int d\Omega_{k'}d\Omega_k Y^*_{lm'}(\hat{k}')Y_{lm}(\hat{k})T_{\beta\alpha}(\mathbf{k}',\mu';\mathbf{k},\mu), \tag{20}$$

$$T^{l\pm}_{\alpha\alpha}(k_{0\alpha},k_{0\alpha}) = \frac{-e^{i\delta_{l\pm}}\sin\delta_{l\pm}}{2\mu_\alpha k_{0\alpha}}, \tag{21}$$

where $x = \cos\theta_{kk'}$, $n = \hat{k}\times\hat{k}'$, and $T^{l\pm}$ is shorthand for $T^{j=l\pm\frac{1}{2}}$. The partial wave expansion for the potential $V_{\beta\alpha}(\mathbf{k}',\mu';\mathbf{k},\mu)$ has the same form as that for $T_{\beta\alpha}(\mathbf{k}',\mu';\mathbf{k},\mu)$ (19), and so, for example, the projection for the potential is

$$V^{lj}_{\beta\alpha}(k',k) = \frac{\pi}{2}\sum_{m,m,\mu\mu'} \langle lm';\tfrac{1}{2}\mu'|l\tfrac{1}{2};jM\rangle\langle lm;\tfrac{1}{2}\mu|l\tfrac{1}{2};jM\rangle \times \int d\Omega_{k'}d\Omega_k Y^*_{lm'}(\hat{k}')Y_{lm}(\hat{k})V_{\beta\alpha}(\mathbf{k}',\mu';\mathbf{k},\mu). \tag{22}$$

After substitution of the partial wave expansions of T and V into (15), we obtain the coupled one-dimensional integral equations

$$T^{lj}_{\beta\alpha}(k',k) = V^{lj}_{\beta\alpha}(k',k) + \frac{2}{\pi}\sum_\gamma \int_0^\infty dp\, \frac{p^2 V^{lj}_{\beta\gamma}(k',p)T^{lj}_{\gamma\alpha}(p,k)}{E+i\epsilon-E_\gamma(k)}. \tag{23}$$

We indicated in Eq. (14) that even for zero kinetic energy (the 1432 MeV threshold), a $\bar{K}N$ pair couples to nearby strangeness -1 charge channels. To use the derived potentials, we evaluate their matrix elements between charge states which in turn are expanded in the isospin states of those channels:

$$\begin{aligned}
|K^-p\rangle &= \tfrac{1}{\sqrt{2}}|0,0\rangle + \tfrac{1}{\sqrt{2}}|1,0\rangle,\\
|\bar{K}^0n\rangle &= \tfrac{-1}{\sqrt{2}}|0,0\rangle + \tfrac{1}{\sqrt{2}}|1,0\rangle,\\
|\Sigma^-\pi^+\rangle &= \tfrac{1}{\sqrt{3}}|0,0\rangle' - \tfrac{1}{\sqrt{2}}|1,0\rangle' + \tfrac{1}{\sqrt{6}}|2,0\rangle,\\
|\Sigma^0\pi^0\rangle &= \tfrac{-1}{\sqrt{3}}|0,0\rangle' + \tfrac{\sqrt{2}}{\sqrt{3}}|2,0\rangle,\\
|\Sigma^+\pi^-\rangle &= \tfrac{1}{\sqrt{3}}|0,0\rangle' + \tfrac{1}{\sqrt{2}}|1,0\rangle' + \tfrac{1}{\sqrt{6}}|2,0\rangle,\\
|\Lambda\pi^0\rangle &= |1,0\rangle''.
\end{aligned} \tag{24}$$

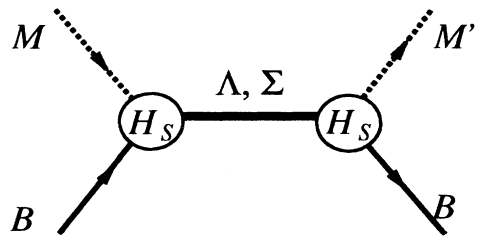

FIG. 2. The Feynman diagram used to generate potentials corresponding to intermediate resonance excitation via the Hamiltonian H_s.

Here the prime and double prime distinguish states with the same isospin but in different particle channels. Because our initial $\bar{K}N$ channel has no isospin-2 component, the $|2,0\rangle$ state does not couple to it and so we eliminate $|2,0\rangle$ and renormalize the rest. Using just two isospin channels for the three $\Sigma\pi$ states reduces computing times by 50%. In order to include some isospin breaking, we do our calculations in the charge basis with physical masses for the particles and use these relations to transform between isospin and charge matrix elements.

To solve the Lippmann-Schwinger equation (23) we have extended the Haftel-Tabakin technique [28] (details in Appendix F). First, rather than work with only the principal part we also keep the delta function (imaginary) part. Also, in handling coupled channels we reorganize the storage of matrices and instead of solving (15) we solve

$$[G^{-1}-V][GT] = [V]. \tag{25}$$

We now can use Gaussian elimination on the symmetric $[G^{-1}-V]$ as opposed to the inversion needed to solve (15). Eliminating inversion saves $\sim 30\%$ in time and utilizing the symmetry of $[V]$ and $[G^{-1}-V]$ saves $\sim 60\%$.

The Coulomb force is included exactly in all our bound state (kaonic hydrogen) calculations, and of course it is crucial there. Even though we have the theoretical tools to include the Coulomb force in scattering, we do not include it in the total cross section calculations because the issue is too confused by different bubble-chamber experiments using different techniques for its removal during analysis. We do include some charge-symmetry-breaking effects by using physical masses, but otherwise we assume isospin is a good symmetry at the field theory and potential level and only break it by using physical masses in the energies for the kaon and lambda channels.

B. Hamiltonian

We deduce the Hamiltonian by following the canonical procedures starting with the energy-momentum tensor $T^{\mu\nu}$ [16,17]:

$$T^{\mu\nu} = \frac{\partial\mathcal{L}}{\partial(\partial_\mu q)}\partial^\nu q + \partial^\nu\bar{q}\frac{\partial\mathcal{L}}{\partial(\partial_\mu\bar{q})} + \frac{\partial\mathcal{L}}{\partial(\partial_\mu\vec{\phi})}\partial^\nu\vec{\phi} - g^{\mu\nu}\mathcal{L}, \tag{26}$$

$$\hat{H} = \int d^3x\, T^{00}(x) = \hat{H}_0 + \hat{H}_s + \hat{H}_c, \tag{27}$$

$$\hat{H}_0 = \hat{H}_{\rm MIT} + \hat{H}_M, \tag{28}$$

$$\hat{H}_s = -\int d^3x\, \frac{\theta_v}{2f}\bar{q}\gamma^\mu\gamma_5\vec{\lambda}q\partial_\mu\vec{\phi}, \tag{29}$$

$$\hat{H}_c = H_{ct} + H_{cs} = \int d^3x \, \frac{\theta_v}{4f^2} \bar{q}\gamma^0 \vec{\lambda} \cdot (\vec{\phi} \times \partial_0 \vec{\phi}) q + \int d^3x \, \frac{\theta_v}{4f^2} \bar{q} \sum_i^3 \gamma^i \vec{\lambda} \cdot (\vec{\phi} \times \partial_i \vec{\phi}) q. \tag{30}$$

Here $\hat{H}_{\rm MIT}$ is the free bag Hamiltonian, $\hat{H}_M$ is the free meson Hamiltonian, $\hat{H}_s$ is the s-channel interaction [Fig. 1(a)], and $(\hat{H}_{ct}, \hat{H}_{cs}]$ are the time and space derivative parts of the contact or four-point interaction [Fig. 1(b)]. We convert $\hat{H}_0$ into the Foch-space form H_0, by projecting onto the space of colorless baryons and expressing the meson field $\vec{\phi}$ in terms of annihilation and creation operators [13,12]:

$$H_0 = \sum_{B_0, B_0'} B_0^\dagger \, \langle B_0 | \hat{H}_0 | B_0' \rangle \, B_0' \tag{31}$$

$$= \sum_{B_0} \sqrt{m_{B_0}^2 + k^2} \, B_0^\dagger B_0 + \sum_i \int d^3k \, \omega_k \, a_i^\dagger(\mathbf{k}) a_i(\mathbf{k}). \tag{32}$$

Here B_0 is the annihilation operator for a three-quark bag of type B_0, $|B_0\rangle$ is the bare baryon state, m_{B_0} is the MIT bare bag mass, and $\omega_k = \sqrt{m_M^2 + k^2}$ is the energy of a free meson of momentum k.

C. Resonance potentials

As discussed in Sec. III and illustrated by the Feynman diagram in Fig. 2, for each meson-baryon channel α we include one of the three resonance states $B_0 = \Lambda_{S01}(1405), \Sigma_{P13}(1385)$, or $\Lambda_{D03}(1520)$. As indicated in Eq. (18), we build potentials containing resonances within them by evaluating this Feynman diagram with the proper initial and final state quark wave functions. In Appendix A we simplify the Hamiltonian H_s which generates these resonances, and in Appendixes B–D we evaluate the contribution to (18) from each of the three resonances. After the partial wave projection there results the potentials

$$v_{\beta\alpha}^{(S01),lj}(k',k) = \delta_{l0}\delta_{j\frac{1}{2}} \frac{u_{\Lambda_{S01}\beta}(k') u_{\Lambda_{S01}\alpha}(k)}{32f^2\pi\sqrt{\omega_{k'}\omega_k}} \frac{\lambda_\beta^\Lambda \lambda_\alpha^\Lambda}{E - M_{S01}} \langle I_{B'} i_{B'}; I_{M'} i_{M'} | I I_{B'} I_{M'}; 00 \rangle \langle I_B i_B; I_M i_M | I_B I_M; 00 \rangle, \tag{33}$$

$$v_{\beta\alpha}^{(D03),lj}(k',k) = \delta_{l2}\delta_{j\frac{3}{2}} \frac{u_{\Lambda_{D03}\beta}(k') u_{\Lambda_{D03}\alpha}(k)}{32f^2\pi\sqrt{\omega_{k'}\omega_k}} \frac{\lambda_\beta^\Lambda \lambda_\alpha^\Lambda}{E - M_{D03}} \langle I_{B'} i_{B'}; I_{M'} i_{M'} | I_{B'} I_{M'}; 00 \rangle \langle I_B i_B; I_M i_M | I_B I_M; 00 \rangle, \tag{34}$$

$$v_{\beta\alpha}^{(P13),lj}(k',k) = \delta_{l1}\delta_{j\frac{3}{2}} \frac{[N_s R \, j_0(\omega_s R)]^4}{24f^2\pi} \frac{\lambda_\beta^\Sigma \lambda_\alpha^\Sigma}{E - M_{P13}} \frac{j_1(k'R) j_1(kR)}{\sqrt{\omega_{k'}\omega_k}} \langle I_{B'} i_{B'}; I_{M'} i_{M'} | I_{B'} I_{M'}; 10 \rangle \langle I_B i_B; I_M i_M | I_B I_M; 10 \rangle. \tag{35}$$

The vertex functions $u_{B_0\alpha}(k)$ for the S and D resonances are seen in the appendixes to be proportional to integrals over spherical Bessel functions (quark wave functions); for Σ_{P13} that substitution is already made in (35). The potentials (33)–(35) are clearly separable and energy dependent. Further, each contains a pole at the real energy $E = M_{B_0}$ arising from the elementary resonances we have explicitly incorporated. As discussed in Sec. III, for any value of M_{B_0} the T matrices generated by using these potentials in the Lippmann-Schwinger equation will have poles at complex energies whose real parts differ from the M_{B_0}'s; that is, the resonances get dressed and acquire widths. In addition, because the values for M_{B_0} are determined by the data fitting, their best-fit values will differ from those we use as input.

D. Contact potentials $v^{(ct)}$, $v^{(cs)}$

As shown in Fig. 1(b), the contact interaction H_c (30) directly produces $BM \to B'M'$ scattering arising from an elementary quark transition [16]. Because B' and B belong to the baryon octet, the quarks in the initial and final states must be in $1s$ states. We break the contact potential into the two pieces $v^{(ct)}$ and $v^{(cs)}$ which are the matrix elements of the time derivative and space derivative parts of H_c:

$$v_{\beta\alpha}^{ct,cs}(\mathbf{k}', \mu', \mathbf{k}, \mu) = \langle \beta, \mathbf{k}', \mu' | H_{ct,cs} | \alpha, \mathbf{k}, \mu \rangle. \tag{36}$$

For S waves the evaluation is straightforward:

$$v^{(cs)}(\mathbf{k}, \mathbf{k}') = 0 \quad (S \text{ wave}), \tag{37}$$

$$v_{\beta\alpha}^{(ct)}(\mathbf{k}', \mathbf{k}) = \sum_I \lambda_{\beta\alpha}^{t,I} \langle I_{B'} i_{B'}; I_{M'} i_{M'} | I_{B'} I_{M'}; I0 \rangle \langle I_B i_B; I_M i_M | I_B I_M; I0 \rangle \frac{u_{\beta\alpha}^{(ct)}(k',k)}{16f^2\pi^3\sqrt{\omega_{k'}\omega_k}}, \tag{38}$$

$$u_{\beta\alpha}^{(ct)}(k',k) = N_s^2(\omega_k + \omega_{k'}) \int_0^R dr \, r^2 \left[j_0^2(\omega_s r) + j_1^2(\omega_s r) \right] j_0(kr) j_0(k'r). \tag{39}$$

The coupling constants $\lambda_{\beta\alpha}^{t,I}$ follow from the SU(6) wave function of the baryon octet [29], and are given in Table II.

TABLE II. The coupling constants λ_α^Λ and λ_α^Σ for channel α, and spacetime coupling constants $(\lambda_{\beta\alpha}^{t,I}, \lambda_{\beta\alpha}^{s,I})$ for channels α and β.

	λ_α^Λ	λ_α^Σ	$(\lambda_{\beta\alpha}^{t,I=0}, \lambda_{\beta\alpha}^{s,I=0})$			$(\lambda_{\beta\alpha}^{t,I=1}, \lambda_{\beta\alpha}^{s,I=1})$		
			$\bar{K}N$	$\Sigma\pi$	$\Lambda\pi$	$\bar{K}N$	$\Sigma\pi$	$\Lambda\pi$
$\bar{K}N$	$\sqrt{2}$	$\sqrt{\frac{8}{3}}$	$(-\frac{3}{2}, -\frac{3}{2})$	$(-\frac{\sqrt{6}}{4}, \frac{1}{2\sqrt{6}})$	$(0,0)$	$(-\frac{1}{2}, \frac{1}{6})$	$(-\frac{1}{2}, \frac{1}{6})$	$(\frac{\sqrt{6}}{4}, \frac{\sqrt{6}}{4})$
$\Sigma\pi$	$\sqrt{3}$	$-\sqrt{\frac{8}{3}}$	$(-\frac{\sqrt{6}}{4}, \frac{1}{2\sqrt{6}})$	$(-2, -\frac{4}{3})$	$(0,0)$	$(-\frac{1}{2}, \frac{1}{6})$	$(-1, -\frac{2}{3})$	$(0, -\frac{2}{\sqrt{6}})$
$\Lambda\pi$	0	2	$(0,0)$	$(0,0)$	$(0,0)$	$(\frac{\sqrt{6}}{4}, \frac{\sqrt{6}}{4})$	$(0, -\frac{2}{\sqrt{6}})$	$(0,0)$

The increased spin and angular momentum coupling in P and D waves makes the vertex functions more complicated. The time derivative part is

$$v_{\beta\alpha}^{(ct)}(\mathbf{k}', \mathbf{k}) = \frac{-i}{64 f^2 \pi^3 \sqrt{\omega_{k'} \omega_k}} {}^{\rm sf}\left\langle B' \left| \int d^3x \theta_v \bar{q}_{1s} f_{i'ij} \lambda_j (\omega_k + \omega_{k'}) \gamma^0 e^{i(\mathbf{k}-\mathbf{k}')\cdot\mathbf{r}} q_{1s} \right| B \right\rangle^{\rm sf}. \tag{40}$$

We evaluate it by substituting the $1s$ quark wave function (B1), substituting the partial wave expansion of the plane wave, and integrating over solid angles to obtain

$$\begin{aligned} v_{\beta\alpha}^{(ct)}(\mathbf{k}'\mu', \mathbf{k}\mu) = \delta_{\mu'\mu} \frac{\omega_k + \omega_{k'}}{8 f^2 \pi^2 \sqrt{\omega_k \omega_{k'}}} \sum_{lm} Y_{lm}^*(\hat{k}) Y_{lm}(\hat{k}') N_s^2 \int_0^R dr\, r^2 [j_0^2(\omega_s r) + j_1^2(\omega_s r)] j_l(kr) j_l(k'r) \\ \times \sum_I \lambda_{\beta\alpha}^{t,I} \langle I_{B'} i_{B'}; I_{M'} i_{M'} | I_{B'} I_{M'}; I0 \rangle \langle I_B i_B; I_M i_M | I_B I_M; I0 \rangle. \end{aligned} \tag{41}$$

The partial wave matrix elements follow from the definition (22):

$$\begin{aligned} v_{\beta\alpha}^{(ct),lj}(k', k) = \frac{N_s^2 (\omega_k + \omega_k')}{16\pi f^2 \sqrt{\omega_{k'} \omega_k}} \int_0^R dr\, r^2 [j_0^2(\omega_s r) + j_1^2(\omega_s r)] j_l(kr) j_l(k'r) \\ \times \sum_I \langle I_{B'} i_{B'}; I_{M'} i_{M'} | I_{B'} I_{M'}; Ii \rangle \lambda_{\beta\alpha}^{t,I} \langle I_B i_B; I_M i_M | I_B I_M; Ii \rangle. \end{aligned} \tag{42}$$

The derivation of the space derivative part $v_{\beta\alpha}^{(cs)}(\mathbf{k}', \mathbf{k})$ is more complicated than the time derivative part and we outline in Appendix E how

$$\begin{aligned} v_{\beta\alpha}^{(cs),lj}(k', k) = \frac{A_l^j N_s^2}{4\pi f^2 \sqrt{\omega_{k'} \omega_k}} \int_0^R dr\, r j_0(\omega_s r) j_1(\omega_s r) j_l(kr) j_l(k'r) \\ \times \sum_I \langle I_{B'} i_{B'}; I_{M'} i_{M'} | I_{B'} I_{M'}; Ii \rangle \lambda_{\beta\alpha}^{s,I} \langle I_B i_B; I_M i_M | I_B I_M; Ii \rangle, \end{aligned} \tag{43}$$

$$A_l^j = 2\sqrt{6l(l+1)(2l+1)}\,(-1)^{j+l+\frac{3}{2}} \begin{Bmatrix} \frac{1}{2} & \frac{1}{2} & 1 \\ l & l & j \end{Bmatrix} = \begin{cases} 2(l+1), & j = l - \frac{1}{2}, \\ -2l, & j = l + \frac{1}{2}. \end{cases} \tag{44}$$

The contact potentials (38), (42), and (43) all are manifestly separable, energy (ω) dependent, and contain vertex factors arising from the quark wave functions. They do not contain elementary resonances, although we will find them to be strong enough to generate composite resonances.

IV. COMPARISON WITH EXPERIMENT

We test the CBM by seeing how well we can reproduce five different groups of data after adjusting seven parameters: the bag radius R, the coupling constants $(f^{I=0}, f_{\bar{K}}^{I=1}, f_\pi^{I=1})$, and the bare masses $(M_{S01}, M_{P13}, M_{D03})$. In comparison to potential models with adjustable coupling constants and ranges, the CBM's SU(3)×SU(3) symmetry greatly reduces the number of parameters—especially since the bare mass values mainly affect the local position of resonance peaks.

A. Scattering and reaction cross sections

The first and largest data group is 300 measurements of two-body scattering and reaction cross sections for

($70 \leq K_{\rm lab} \leq 513$) MeV/$c$ $\equiv$ ($1435 \leq E_{\rm c.m.} \leq 1567$ MeV) [26,30–36]. These data, shown in Figs. 3–5, are predominantly from bubble chambers and contain rather large statistical and systematic errors. The extension of the cloudy bag model to higher partial waves is important for understanding these data since even for a K^- momentum as low as 150 MeV/c, P-wave contributions to $K^-p \to \Sigma^{\mp}\pi^{\pm}$ have been reported [26], and at 390 MeV/c there is the $\Lambda(1520)$ D-wave resonance (the peak evident in the figures near 400 MeV/c) [30].

The cross sections are related to the computed T-matrix elements (23) by

$$\frac{d\sigma_{\beta\alpha}}{d\Omega} = 16\pi^4 \mu_\beta \mu_\alpha \frac{k'}{k} \overline{\sum_{\mu',\mu}} \left|T_{\beta\alpha}(\mathbf{k}'\mu', \mathbf{k}\mu)\right|^2 , \tag{45}$$

$$\sigma_{\beta\alpha} = \int d\Omega \, \frac{d\sigma}{d\Omega} = 16\pi \mu_\beta \mu_\alpha \frac{k'}{k} \sum_{l=0}^{\infty} \left[(l+1)\left|T^{l+}_{\beta\alpha}(k',k)\right|^2 + l\left|T^{l-}_{\beta\alpha}(k',k)\right|^2\right] . \tag{46}$$

Here the overbar indicates a sum over final and average over initial spin states, and the μ_α's are relativistic reduced channel masses defined in Eq. (F3). For the channels we use the integrated cross sections are

$$\sigma(K^-p \to K^-p) = 16\pi\mu_1^2 \sum_{l=0}^{2} \left[(l+1)\left|T^{l+}_{11}(k',k)\right|^2 + l\left|T^{l-}_{11}(k',k)\right|^2\right] , \tag{47}$$

$$\sigma(K^-p \to \bar{K}^0 n) = 16\pi\mu_1\mu_2 \frac{k'}{k} \sum_{l=0}^{2} \left[(l+1)\left|T^{l+}_{21}(k',k)\right|^2 + l\left|T^{l-}_{21}(k',k)\right|^2\right] , \tag{48}$$

$$\begin{aligned}\sigma(K^-p \to \Sigma^+\pi^-) = 16\pi\mu_3\mu_1 \frac{k'}{k} \sum_{l=0}^{2} \Bigg[&(l+1)\left|\frac{1}{\sqrt{3}}T^{l+}_{31}(k',k) + \frac{1}{\sqrt{2}}T^{l+}_{41}(k',k)\right|^2 \\ &+ l\left|\frac{1}{\sqrt{3}}T^{l-}_{31}(k',k) + \frac{1}{\sqrt{2}}T^{l-}_{41}(k',k)\right|^2\Bigg] ,\end{aligned} \tag{49}$$

$$\sigma(K^-p \to \Sigma^0\pi^0) = 16\pi\mu_3\mu_1 \frac{k'}{k} \sum_{l=0}^{2} \left[(l+1)\left|\frac{1}{\sqrt{3}}T^{l+}_{31}(k',k)\right|^2 + l\left|\frac{1}{\sqrt{3}}T^{l-}_{31}(k',k)\right|^2\right] , \tag{50}$$

$$\begin{aligned}\sigma(K^-p \to \Sigma^-\pi^+) = 16\pi\mu_3\mu_1 \frac{k'}{k} \sum_{l=0}^{2} \Bigg[&(l+1)\left|\frac{1}{\sqrt{3}}T^{l+}_{31}(k',k) - \frac{1}{\sqrt{2}}T^{l+}_{41}(k',k)\right|^2 \\ &+ l\left|\frac{1}{\sqrt{3}}T^{l-}_{31}(k',k) - \frac{1}{\sqrt{2}}T^{l-}_{41}(k',k)\right|^2\Bigg] ,\end{aligned} \tag{51}$$

$$\sigma(K^-p \to \pi^0\Lambda) = 16\pi\mu_5\mu_1 \frac{k'}{k} \sum_{l=0}^{2} \left[(l+1)\left|T^{l+}_{51}(k',k)\right|^2 + l\left|T^{l-}_{51}(k',k)\right|^2\right] . \tag{52}$$

B. $\Lambda(1405)$ resonance

The second data group we examine is seven values of the $\Sigma^+\pi^-$ mass spectrum determined from the $K^-p \to \Sigma^+\pi^-\pi^+\pi^-$ reaction at 4.2 GeV/c kaon laboratory momentum by Hemingway [37]. These data, shown in Figs. 3–5, have a strong $\Lambda(1405)$ resonance signal and are a major constraint on the model's parameters. Earlier $\Lambda(1405)$ data also exist, but Hemingway's are cleaner since they were obtained through the three-step process $K^-p \to \Sigma^+\pi^-$, $\Sigma^+ \to \Lambda(1405)\pi^+$, $\Lambda(1405) \to \Sigma^0\pi^0$. We calculate the $\Sigma\pi$ mass spectrum with a Watson model [30,38] which assumes that an S-wave resonance dominates the final state interaction. The number of events per unit energy interval is accordingly

$$\frac{dN}{dE} \propto k\,\sigma_{\Sigma\pi\to\Sigma\pi} \propto k\mu_3^2 \left|T^0_{33}(k,k)\right|^2 . \tag{53}$$

We fix the normalization by setting the area under the theoretical mass spectrum equal to the total number of events. Because this model is so simple, we do not expect a detailed reproduction of the spectrum.

C. $\Sigma(1385)$ resonance

The $\Sigma(1385)$ is seen as a P-wave $\pi^0\Lambda$ resonance below the $\bar{K}N$ threshold. Aguilar-Benitez and Salicio [39] have detected it in the mass spectrum from $K^-p \to \Lambda\pi^0\pi^+\pi^-$ at 4.2 GeV/c. Our calculation of that $\Lambda\pi$ spectrum is

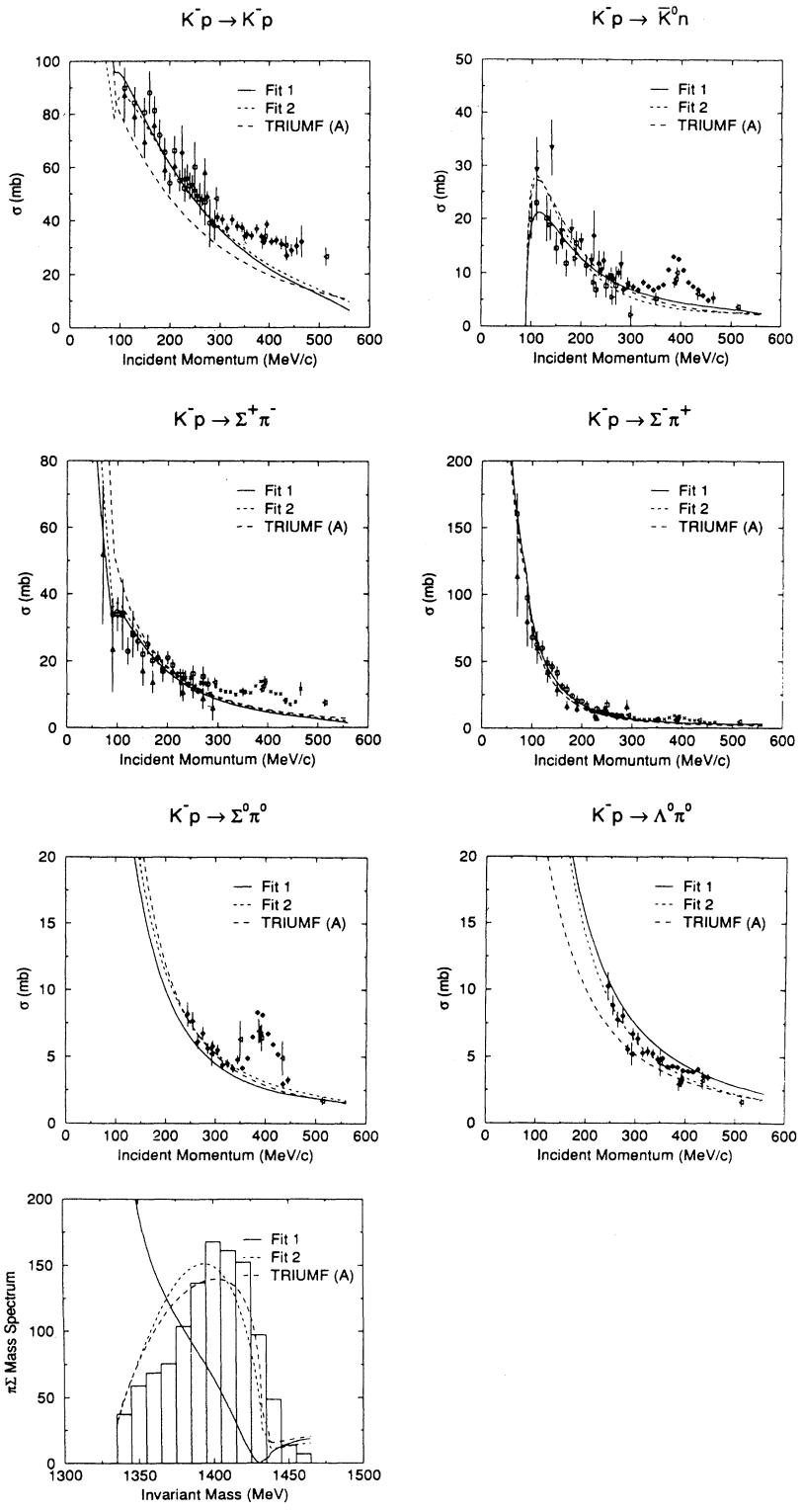

FIG. 3. The K^-p scattering cross sections, reaction cross sections, and $\Sigma\pi$ mass spectrum calculated with the S-wave fits 1, 2, and TRIUMF (A). As is evident, fit 1 was not adjusted to fit the mass spectrum. The cusps right below 100 MeV/c arise from the opening of the $\bar{K}^0N$ channel, and the peaks near 400 MeV/c arise from the $\Lambda(1520)$ D-wave resonance (not included in these S-wave fits). The cross section data are ○: Cibrowski *et al.* [26]; □: Kim [32]; ◇: Mast *et al.* [34]; △: Sakitt *et al.* [31]; ◁: Watson *et al.* [30]; ▽: Evans *et al.* [36]; ▷: Kittel *et al.* [33]; and ×: Bangerter *et al.* [35]. The $\Sigma\pi$ mass spectrum is from Hemingway [37].

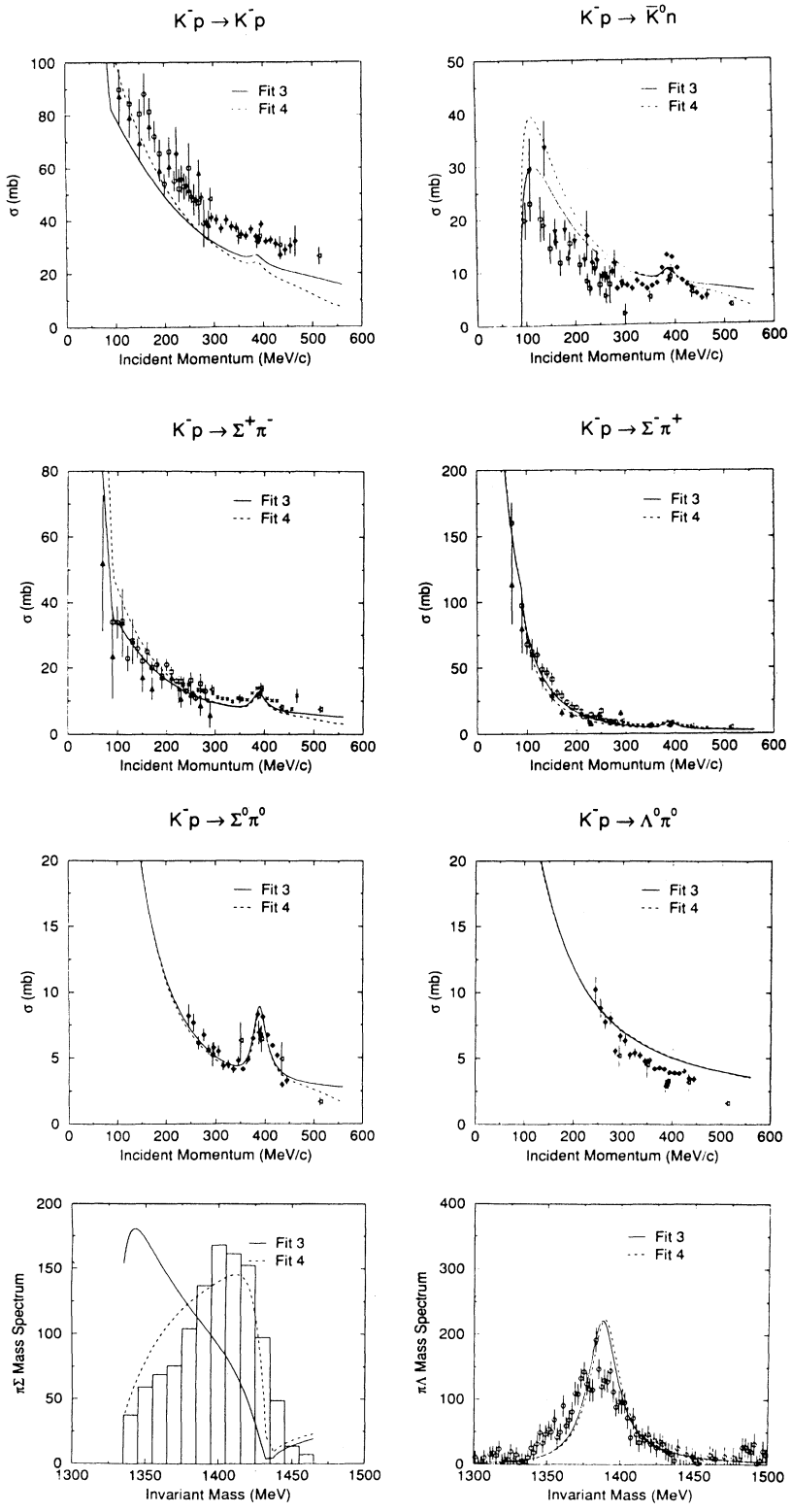

FIG. 4. The K^-p scattering cross sections, reaction cross sections, $\Sigma\pi$ mass spectrum, and $\pi^0\Lambda^0$ mass spectrum calculated with parameters of fits 3 and 4. Both fits include S, P, and D waves, but fit 4 was not adjusted to branching ratios (shown in Fig. 6). The cross section data are the same as in Fig. 3 with the addition of the $\pi^0\Lambda^0$ mass spectrum extracted from the results of Aguilar-Benitez and Salicio [39].

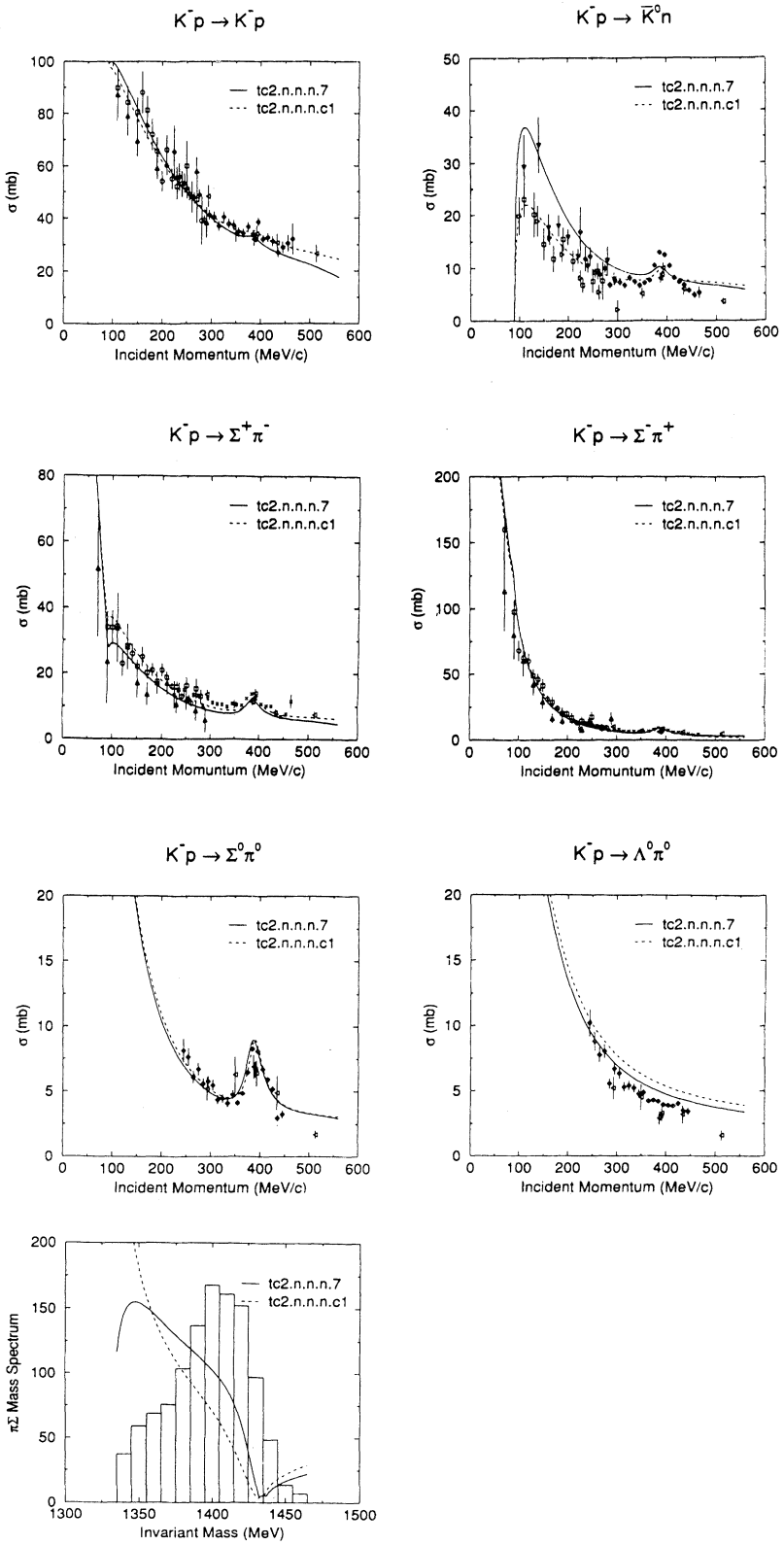

FIG. 5. The K^-p scattering cross sections, reaction cross sections, and $\Sigma\pi$ mass spectrum calculated with parameters of fits $n7$ and $c1$. Both fits include S, P, and D waves, but were not adjusted to mass spectra data. Fit $c1$ used equal weights for the data in the χ^2 minimum search. The cross sections data are same as in Fig. 4.

similar to the $\Sigma\pi$ calculation, only now with the Watson final state interaction model adapted to a P-wave resonance:

$$\frac{dN}{dE} \propto \frac{\sigma_{\Lambda\pi\to\Lambda\pi}}{k} \propto \frac{\mu_5^2}{k}\left|T_{55}^{1+}(k,k)\right|^2. \quad (54)$$

Because the resonance rests upon a large background, and because we have no model for such a background, we extract the resonance piece after fitting the entire spectrum as a polynomial background plus a Breit-Wigner resonance [39]:

$$\frac{dN}{dM} = a_0 + a_1\left(\frac{M}{M_0}\right) + a_2\left(\frac{M}{M_0}\right)^2 + \frac{bM_0^2\Gamma_0^2}{(M-M_0)^2+M_0^2\Gamma^2}, \quad (55)$$

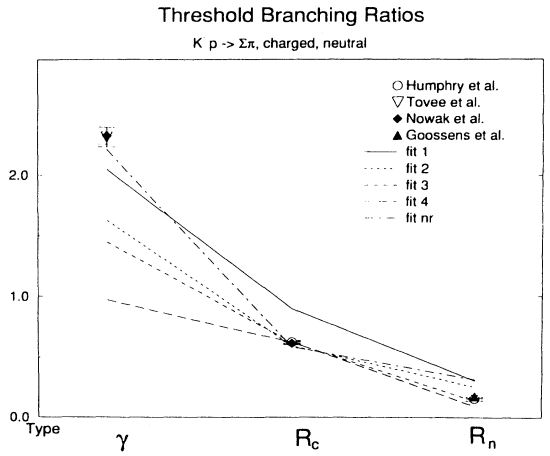

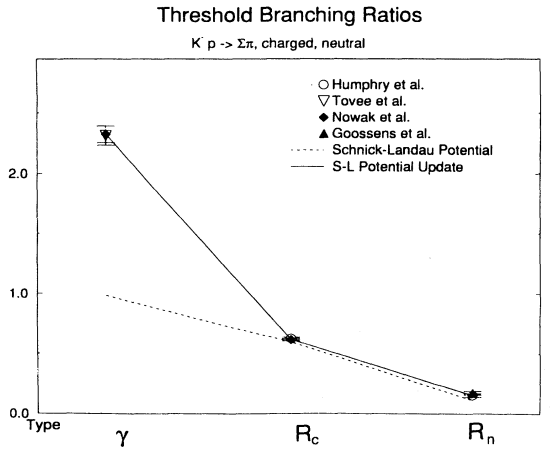

FIG. 6. The threshold branching ratios for K^-p to neutral states R_n, to charged states R_c, and to charged $\Sigma\pi$ states γ. The comparisons in the top part of the figure indicate that CBM fits adjusted to the $\Sigma\pi$ mass spectrum tend not to agree with γ. The comparisons in the bottom indicate that the original Schnick-Landau potential parameters [23] did not provide good agreement for γ, but the update (solid curve) by Tanaka and Suzuki [24] does. The data are from Humphrey and Ross [40], Tovee *et al.* [41], Nowak *et al.* [42], and Goossens *et al.* [43].

$$\begin{aligned}(M,\Gamma) &= (1384, 34.8)\ \text{MeV},\\ a_{0,1,2} &= (-77554, 15303, -7402)\ \text{MeV},\\ b &= 158.7\text{MeV}^{-4}.\end{aligned} \quad (56)$$

The resulting resonance is shown in Fig. 4 as the peak at 1385 MeV.

D. K^-p threshold branching ratios

The third group of data we examine is the branching ratios of K^-p reaction rates at threshold:

$$\gamma = \frac{K^-p\to\Sigma^-\pi^+}{K^-p\to\Sigma^+\pi^-},\quad R_c = \frac{K^-p\to\text{charged}}{K^-p\to\text{all}},\quad R_n = \frac{K^-p\to\pi^0\Lambda}{K^-p\to\text{neutral}}. \quad (57)$$

The measured ratios [40–43] are shown in Fig. 6. The attraction of ratios is that they are not affected by uncertainties in target size and beam normalization, and so their uncertainties are smaller than those of cross sections. The difficulty is that calculations of rates into charge channels at zero energy are sensitive to Coulomb and charge-symmetry-breaking effects—not all of which are included in our model—and so we cannot be sure of the level of agreement to expect.

E. Data fitting

We have tried a variety of fitting procedures (indicated in Table III) in which different groups of data were systematically included and excluded, and with different choices for the χ^2 weights for each. The parameters of our model determined by various fits to these data groups are given in Table IV. The comparisons with the cross section and mass data are in Figs. 3–5, and the experimental and theoretical branching ratios are in Fig. 6. The data groups have large differences in the number of data points, the type of data, and the accuracy of the error estimates. Accordingly, it was not clear to us how properly to perform a best fit to all groups simultaneously.

In Fig. 3 we see fit 1. It employs only S waves and has its parameters adjusted to fit the low-energy ($p \le 250$ MeV/c, $E \le 1470$ MeV) two-body scattering and re-

TABLE III. Characteristics of different fits.

Fit	S	P, D	$M(\Sigma\pi)$	$M(\Lambda\pi)$	BR	χ^2
1	√	×	×	×	×	$\Delta\sigma$
2	√	×	√	×	×	$\Delta\sigma$
Tri	√	×	√	×	×	$\Delta\sigma$
3	√	√	√	√	√	$\Delta\sigma$
4	√	√	√	√	×	m
n7	√	√	×	×	×	$\Delta\sigma$
c1	√	√	×	×	×	m

TABLE IV. Parameters of different fits; R is in fm, others in MeV.

Fit	R	M_{S01}	M_{P13}	M_{D03}	$f^{I=0}$	$f_K^{I=1}$	$f_\pi^{I=1}$
1	1.29	1554			87	80	75
2	0.95	1588			126	82	146
Tri	1.00	1630			120	100	110
3	1.23	1577	1421	1558	96	100	79
4	1.32	1542	1417	1546	103	96	78
add1	1.34	1564	-1249	1553	92	80	88
add2	1.19	1623	-12682	1568	90	87	80

action cross sections. This fit provides a good base for comparison with the results of other groups and with our latter results in which higher partial waves are included. Fit 2 is also an S-wave fit to low-energy data, but extends fit 1 by including the $\Sigma\pi$ mass spectrum with its $\Lambda_{S01}(1405)$ resonance. The fit labeled TRIUMF (A) uses the CBM parameter set A given by Veit *et al.* [16] and uses the same criteria as our fit 2. Fit 2 and TRIUMF produce somewhat different parameters (row 1 vs 3 in Table IV) due to differences in procedures and data.

We see in Fig. 3 how much better an agreement fit 2 provides with the $\Sigma\pi$ mass spectrum than fit 1, and in Table IV the large extent to which inclusion of the $\Sigma\pi$ spectrum affects the model's parameters. In examining the predictions for the branching ratios in the top part of Fig. 6, we notice that fit 1 provides close agreement with R_n and R_c, and fairly close agreement with γ. However, fit 2, which also included the $\Sigma\pi$ mass spectrum in its fitting, provides noticeably worse agreement with γ. For contrast, in the bottom part of Fig. 6 we present the branching ratios calculated with the Schnick-Landau potential model [23]. We see that the updated parameters determined by Tanaka and Suzuki [24] provide excellent agreement with the ratios.

In Fig. 3 we notice that all three S-wave fits fail to obtain agreement with the data at higher energies, and in particular, they fail to reproduce the $\Lambda_{D03}(1520)$ resonance signal at 400 MeV/c. This clearly shows the need for higher partial waves and additional resonances.

Our next two fits are shown in Fig. 4. Fit 3 uses S, P, and D waves, examines data at higher momenta, and includes the three mass spectra for the $\Lambda_{S01}(1405)$, $\Sigma_{P13}(1385)$, and $\Lambda_{D03}(1520)$ resonances. To determine the influence of the branching ratio data and to deemphasize the $\Sigma\pi$ spectrum, in fit 4 we do not fit to branching ratios and manually (m in Table III) set the χ^2 weight factors to $(w_{\text{scattering}}, w_{\Sigma\pi}, w_{\Lambda\pi}) = (6, 1, 6)$.

It is interesting to note in Fig. 4 that fits 3 and 4, which include S-D waves, do not provide as good agreement with the $K^-p \to (K^-p, \bar{K}^0n, \Lambda^0\pi^0)$ elastic cross sections as the S-wave fits 1 and 2. What is clear from the figure, however, is that fits 3 and 4 provide nearly perfect agreement with the $K^-p \to \Sigma\pi$ cross sections; apparently the large number of high-energy, small-error, $\Sigma\pi$ data points dominates these fits. This analysis is confirmed by confirming that the fit with the high-energy data have a lower χ^2 per degree of freedom.

We again see in the $\Sigma\pi$ mass spectrum of Fig. 4 that fit 3 (which was adjusted to fit the branching ratios) does not produce a good $\Sigma\pi$ mass spectrum. Yet by releasing the branching ratio constraint we obtain fit 4—which agrees with the spectra quite well. We also see that both fits do provide fairly good agreement with the $\pi\Lambda$ mass spectrum. This spectrum shows the sub-$\bar{K}N$-threshold $\Sigma_{P13}(1385)$ resonance and essentially determines the value for M_{P13}.

It can be argued that because so many assumptions go into applying the Watson final state interaction model to fit the various mass spectra, we should not expect good agreement with those spectra, and so should not use the spectra in data fitting. For these reasons, in fits $n7$ and $c1$ we used all partial waves but fit only the two-body scattering and reaction data; $n7$ has weights determined by the experimental errors, and $c1$ has equal weights so that the small-$\Sigma\pi$ error bars at high energy would have less influence. Again we note that without the $\Sigma\pi$ mass spectrum constraint, very good agreement with the branching ratios is obtained (fit $n7$ in Fig. 6) even though the ratio data were not included in the fit. Yet if the $\Sigma\pi$ mass spectra must be fit, then fit 4 is our best fit even though we see in Fig. 6 that it does not fit the branching ratios well.

Because the $\pi\Lambda$ mass spectrum determines the value for M_{P13}, and because this resonance does not significantly affect the cross section data above the $\bar{K}N$ threshold, not fitting this spectrum means the values for M_{P13} were not determined in fits $n7$ and $c1$. This explains the negative values they have in Table IV. The other resonance masses do affect the cross section data above the $\bar{K}N$ threshold, and reasonable values were obtained for them.

V. SCATTERING AMPLITUDES

Now that the model parameters are determined, for each parameter set we examine the scattering amplitudes as a function of energy. We shall see that these amplitudes often have such a rapid energy dependence, especially near the $\bar{K}N$ threshold, that an examination of the full energy dependence is more significant that just the threshold values (scattering lengths). Values at that one energy are too sensitive to details such as channel mass values [45].

We start in Fig. 7 with the scattering amplitudes for $\bar{K}N \to \bar{K}N$ in the D_{03} channel and for the $\pi\Lambda \to \pi\Lambda$ in P_{13}. As we move down in energy we see vertical bars which signal the $\bar{K}N$ and $\Sigma\pi$ thresholds (the $\pi\Lambda$ threshold at 1252 MeV is not visible). We also see cusps in f at channel openings and that Im f—but not Ref—vanishes when all channels are closed. The $\bar{K}N$ resonance $\Lambda_{D03}(1520)$ and the $\pi\Lambda$ resonance $\Sigma_{P13}(1385)$ are clearly signaled by Ref changing sign and Im f peaking at approximately the energy corresponding to the resonance mass. The bare versions of these resonances were built into our effective potentials via (18), yet this does not guarantee that they will remain after their dressing by the Lippmann-Schwinger equation and the adjustment of parameters in the data fitting.

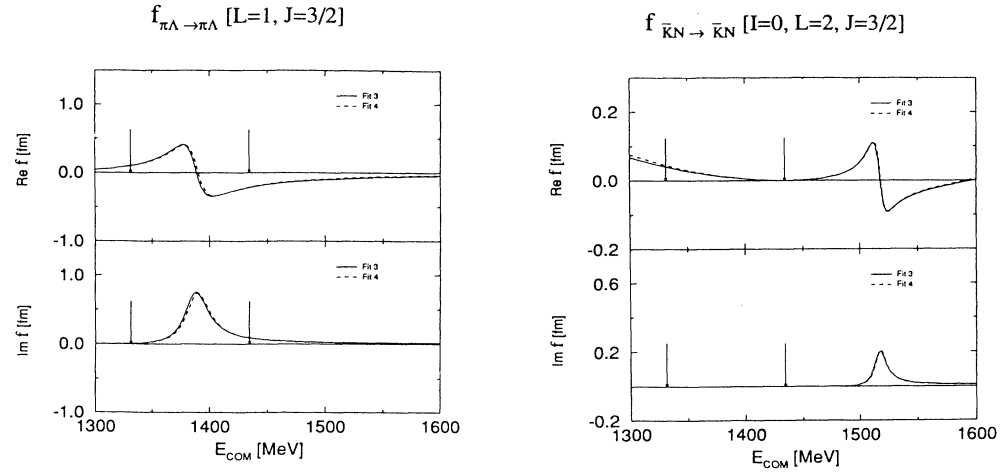

FIG. 7. The P_{13}, $\pi\Lambda$, and D_{03} $\bar{K}N$ scattering amplitudes of fits 3 and 4. The Imf in the lower halfs of the figure peaks at the resonance energy for which the Ref passes through zero in the upper part. The arrows show the $\Sigma\pi$ and $\bar{K}N$ thresholds.

In Fig. 8 we give the $I = 0$, S-wave $\bar{K}N$ scattering amplitude for fits 1–4 and TRIUMF-A (since fit 2 is an updated TRIUMF-A, the two are very similar). We see that fit 1's Ref changes sign once below the $\bar{K}N$ threshold (rightmost arrow in Fig. 8) and once again slightly above the $\Sigma\pi$ threshold (leftmost arrow). All the fits' Ref's pass through or very close to zero above and below the $\bar{K}N$ threshold, but only fit 1's Ref has an extra sign change far below. This is fascinating, for the ability of the model to reproduce the experimental $1S$ strong interaction shift of kaonic hydrogen depends on the magnitude and sign of Ref at threshold, and clearly there are several sign changes here.

The imaginary parts of f (lower part of figure) for fits 1–3 show a shoulder right below the $\bar{K}N$ threshold at $\sim$ 1440 MeV, while fit 4 shows a peak at $\sim$ 1425 MeV. None of these behaviors for Ref and Im f are the classical resonance signal expected at 1405 MeV for the $\Lambda_{S01}(1405)$; although there appears to be a resonance signal somehow mixed into the $\bar{K}N$ threshold behavior. Fits 1 and 3 do show what appears to be distinctive resonance signals in both Ref and Im f, but they appear way down in energy near the $\Sigma\pi$ threshold of 1325 MeV. Clearly, since Table IV shows the fitted $M_{S01} \geq 1550$ MeV, the cloudy bag model does not give the $\Lambda_{S01}(1405)$ as a simple bag state of mass $\simeq$ 1405 MeV.

In order to unravel some of the mysterious resonance behavior of the S_{01} $\bar{K}N$ scattering amplitude, we have solved for the complex energies at which the scattering amplitudes have poles. If the pole is on the second (unphysical) energy sheet near the real positive axis, it will produce an observable, narrow resonance along the positive real energy axis with a width related to the imaginary part of the complex energy by

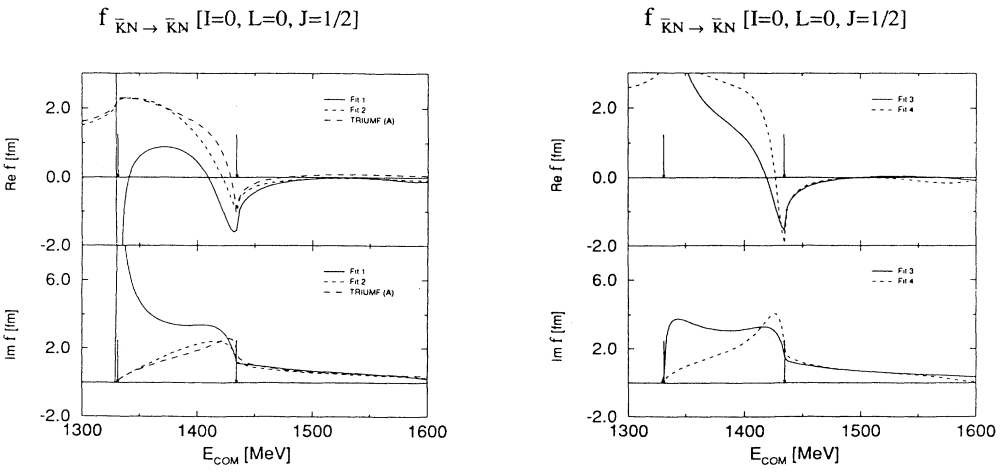

FIG. 8. The $\bar{K}N$ S_{01} scattering amplitudes for fits 1–4. The arrows show the $\Sigma\pi$ and $\bar{K}N$ thresholds. The resonance and threshold behaviors appear mixed.

$$\Gamma \simeq -2\mathrm{Im}\ E. \tag{58}$$

Other singularities or channel openings can interfere with this picture. If the pole is far away from the real energy axis or some other singularity gets in the way, its experimental and dynamical significance is less. In Appendix F we show that the formal solution of the Lippmann-Schwinger equation implies that the pole positions are solutions of the equation

$$\det(1 - V_E G_E) = 0. \tag{59}$$

We find numerically the complex energies which solve (59).

In Fig. 9 we have plots of the imaginary parts of the $\bar{K}N$ S wave scattering amplitudes of fits 2 (upper part of figure) and 3 (lower part of figure) as functions of complex energy. As found in the explicit solution of (59), and evident in the figure, there are two poles in the $S01$ channel at the complex energy listed in Table V. For fit 2 we note that the high-energy pole is actually 17 MeV *above* the $\bar{K}N$ threshold (the tick mark to the right of 1400 MeV in Fig. 9) and 31 MeV along the negative imaginary axis. Fit 2's low-energy pole is seen to be 80 MeV below the $\bar{K}N$ threshold and far from the real energy axis. In contrast, fit 1 and fit 3 (in the lower part of the figure) have low-energy poles very close to the real energy axis. They are the causes of the striking energy dependences near the $\Sigma\pi$ threshold seen in Fig. 8.

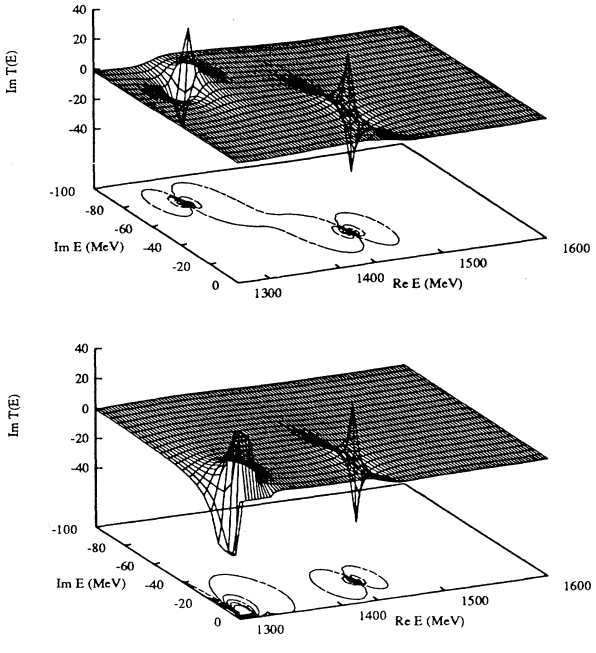

FIG. 9. The imaginary parts of the $\bar{K}N$ S-wave scattering amplitudes of fit 2 (upper part) and fit 3 (lower part) as a function of complex energy. The projection onto the complex energy plane shows the contours of the T matrix. The tick mark to the right of 1400 on the real energy axis is the $\bar{K}N$ threshold energy.

TABLE V. The pole positions in complex energy (in MeV) for S-D waves relative to the $\bar{K}N$ threshold at 1432 MeV. Numerical uncertainty is $\sim \pm 2$ MeV.

Fit	$E(S)$	$E(P)$	$E(D)$
1	(2, -27), (-104, -6×10^{-5})		
2	(17, -31), (-80, -76)		
Tri	(13, -12), (-95, -76)		
V_{r2} [19]	(-52, -39)		
V_{AHW} [44]	(-14, -25)		
3	(5, -21), (-129, -4)	(-48, -12)	(81, -6)
4	(1.2, -13), (-114, -74)	(-46, -12)	(83, -6)

The T matrices' pole positions for the P- and D-wave amplitudes are also listed in Table V. These positions correspond to a $\Sigma_{P13}(1395)$ dressed mass of 1385 MeV and width of 24 MeV, and a $\Lambda_{D03}(1520)$ dressed mass of 1514 MeV and width of 12 MeV. The values for the best-fit bare masses are $M_{P13} \simeq 1419$ MeV and $M_{D03} \simeq 1552$ MeV. This means that in *both* cases the renormalization by the contact interaction and higher order scatterings shift the masses downwards in energy by 31 MeV. The tabulated [48] masses and widths of $(1383.7 \pm 1.0,\ 36 \pm 5)$ MeV and $(1519.5 \pm 1.0,\ 15.6 \pm 1.0)$ MeV are in excellent agreement with the pole positions—especially since the two are expected to differ somewhat when the pole is not close to the real energy axis. The tabulated half widths of the $\Sigma_{P13}(1395)$ and $\Lambda_{D03}(1520)$ are not in as close agreement with the imaginary parts of the pole energies (18 ± 3 vs 12, 8 ± 1.0 vs 6), but this is expected since the widths arise completely from renormalization, and this is a broad and nonsymmetric resonance.

There are three measurements of the width Γ and strong interaction shift relative to Bohr energy, $\epsilon = -(E - E_B)$, of the $1S$ level in kaonic hydrogen [20–22]. Although these measurements should be a good test of the $\bar{K}N$ interaction slightly below threshold, the uncertainties in the measurements make conclusions difficult (we see the statistical uncertainty in Fig. 10, but not the apparent systematic uncertainties). Since at present there is distrust of a theory if it agrees with these experiments, we eagerly await the new experiment in progress with its promise of high precision and high accuracy [49].

In our calculation of the kaonic hydrogen state, we

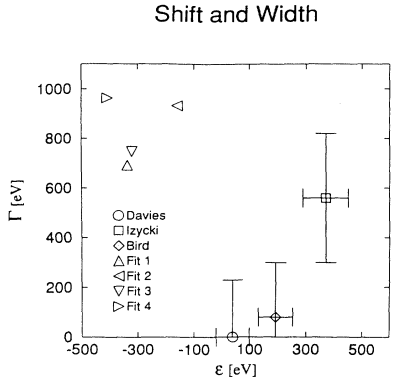

FIG. 10. The shift and width due to the strong interaction of the $1S$ level in kaonic hydrogen. The data are from Davies *et al.* [20], Izycki *et al.* [21], and Bird *et al.* [22]. The triangles are prediction of the different CBM fits. All experiments indicate a positive ϵ while all CBM calculations indicate a negative shift (to the less bound).

identify the complex bound state energy as the T matrix pole energy for the combined Coulomb-plus-nuclear force problem [50], and solve (59) for them. Our predictions are shown in Fig. 10. For all the CBM fits the calculated width Γ is acceptable or slightly large, yet the shift ϵ is of opposite sign to the data (all experimental shifts are to the more bound). If the data are correct, then this implies that the the real part of the K^-p scattering amplitude (a sum of $I=0$ and $I=1$ amplitudes) is positive at K^-p threshold even though the $I=0$ piece dips below zero at threshold. The potential model of Schnick and Landau [23] or its update by Tanaka and Suzuki [24] have this property; that is, they agree in sign with the data. Although the sign changes in some of the cloudy bag model's $\mathrm{Re}f_{S01}$ are similar to those of the potential models, none of our CBM fits have the proper combination of $I=0$ and $I=1$ strengths to keep $\mathrm{Re}f(K^-p)>0$. Although we have not done it, we suspect that if this condition were made a requirement of the search, such a solution would be found (presumably at the expense of other data).

VI. SUMMARY AND CONCLUSIONS

We have extended the SU(3) cloudy bag model for the coupled ($\bar{K}N$, $\Sigma\pi$, $\Lambda\pi$) system from S to D waves and thus to much higher energies. The model has elementary quarks inside a bag as well as an SU(3) meson field inside and outside the bag. While not derived from quarks, the meson field restores chiral symmetry. The model Hamiltonian contains a contact interaction which generates direct meson-baryon scattering as well as an s-channel interaction used to include elementary $\Lambda_{S01}(1405)$, $\Sigma_{P13}(1520)$, and $\Lambda_{D03}(1385)$ resonances. We derived effective, energy-dependent separable potentials for use in the Lippmann-Schwinger equation as well as some new numerical approaches to solve the coupled Lippmann-Schwinger equation. The parameters of the model were determined after extensive fits to various scattering, reaction, branching ratio, and mass spectra data.

Our fitting and subsequent analyses indicate that the $\Sigma(1395)$ and $\Lambda(1520)$ are well described as elementary resonances. Although their pole positions are renormalized by the contact interaction and higher order scatterings from the Lippmann-Schwinger equation to 31 MeV below their bare masses, the resonance energies (as determined by the complex energy poles of the T matrix) are within 2 and 4 MeV respectively of the tabulated values.

The cloudy bag model's description of the $\Lambda(1405)$ S-wave resonance is less simple. While we agree with the previous conclusion that the state is not an elementary, three-quark s-channel resonance [16,19,38,44,46], we have also found that it is less simple than the quasi-bound $\bar{K}N$, single pole state produced by potential models [23,44]. In particular, there are two poles present in this channel, with the resonant behavior near threshold arising from a pole above threshold interfering with the threshold cusp.

Although the two sign changes in some of the cloudy bag model's $\bar{K}N$ scattering amplitude near threshold are quite similar to those of potential models which agree in sign with the strong interaction shift in kaonic hydrogen, none of our CBM fits have quite the proper combination of $I=0$ and $I=1$ strengths to keep $\mathrm{Re}f(K^-p)>0$. Agreement with the shift could be required as part of the fitting procedure, but we suspect that this is best left for a time when more acceptable data are available [49].

In a general sense we conclude that the CBM with S, P, and D waves is able to reproduce the K^-p scattering and reaction cross sections from 70 $\rightarrow$ 513 MeV/c (1435 $\rightarrow$ 1567 MeV) and either the $K^-p \rightarrow (\Sigma\pi\pi\pi, \Lambda\pi\pi\pi)$ mass spectra *or* the branching ratios

$$\gamma = \frac{K^-p \rightarrow \Sigma^-\pi^+}{K^-p \rightarrow \Sigma^+\pi^-}, \quad R_c = \frac{K^-p \rightarrow \text{charged}}{K^-p \rightarrow \text{all}}, \quad R_n = \frac{K^-p \rightarrow \pi^0\Lambda}{K^-p \rightarrow \text{neutral}}. \tag{60}$$

Fitting all three together appears too much to ask from such a simple model.

We note that the fitted parameters appear reasonable. The average bag radius $\overline{R} \simeq 1.22 \pm 0.14$ fm is about 0.1 fm larger than the value found by Veit *et al.* [16], but within the range $1.5 \geq R \geq 1.0$ fm given by Guidry [52] (the range is for simple to refined models, and our model with massless quarks is simple). If we restrict our fit to low-energy scattering and mass spectra data we obtain $R = 0.95$ fm, which is not big and indicates that larger R values arise from the effort to fit the high-energy data. The fitted meson decay constants $(f^{I=0}, f_K^{I=1}, f_\pi^{I=0}) \simeq (99, 88, 91)$ MeV appear quite close to accepted [52] values $(f_K, f_\pi) = (112, 93)$ MeV, especially since SU(3) predicts $f_\pi = f_K$.

In conclusion, we believe the cloudy bag model has success in reproducing much data—but clearly with limits.

The difficulties may arise from trying to reproduce complicated energy dependences with too simple a model. We have kept only linear terms in the meson field and have assumed a rigid and spherical bag of one size for all baryons. The bag does not recoil and the pointlike mesons do not arise from quarks. We expect this to cause difficulties at the higher energies and higher momentum transfers. We have used the MIT bag wave functions for massless quarks in a square well, and so have form factors proportional to spherical Bessel functions. This too is rather restrictive. We have looked at zero-kinetic-energy branching ratios, but have included isospin-breaking effects only at the Lippmann-Schwinger equation level not at the Hamiltonian level. Clearly, all these effects may be important in a more sophisticated study of branching ratios and of the kaonic hydrogen level shifts. Further improvements appear worthwhile as do applications of the model within a nuclear environment.

ACKNOWLEDGMENTS

We wish to thank Al Stetz, Byron Jennings, Jeffrey Schnick, Tony Thomas, Iraj Afnan, Gerry Miller, Mary Alberg, Larry Wilets, and Ernest Henley for stimulating and illuminating discussions. We also wish to gratefully acknowledge support from the U.S. Department of Energy under Grant No. DE-FG06-86ER40283, and the people at the National Institute for Nuclear Theory, Seattle for their hospitality during part of this work.

APPENDIX A: REDUCTION OF H_S

We convert $\hat{H}_s$ (29) into a more calculable form by partial integration:

$$\hat{H}_s = -\int d^3x \left\{ \partial_\mu \left[\frac{\theta_v}{2f} \bar{q}\gamma^\mu\gamma_5 \vec{\lambda} q \cdot \vec{\phi} \right] - \frac{(\partial_\mu \theta_v)}{2f} \bar{q}\gamma^\mu\gamma_5 \vec{\lambda} q \cdot \vec{\phi} - \frac{\theta_v}{2f} \partial_\mu \left[\bar{q}\gamma^\mu\gamma_5 \vec{\lambda} q \right] \cdot \vec{\phi} \right\}. \tag{A1}$$

Application of the Dirac equation for the bag (2) shows the last term to vanish. The space derivative in the first term is converted to a surface integration over a infinitely large surface, which in turn vanishes since the quark field is confined within the bag. The linear boundary condition (3) and the surface delta function imply $-(\partial_\mu\theta_v)\bar{q}\gamma^\mu\gamma_5\vec{\lambda}q\cdot\vec{\phi}/2f = -\frac{i}{2f}\delta_s\bar{q}\gamma_5\vec{\lambda}q\cdot\phi$ and this yields

$$\hat{H}_s = \int d^3x \left[\frac{i}{2f} \bar{q}\gamma_5 \vec{\lambda}\cdot q\vec{\phi}\delta_s - \frac{\theta_v}{2f} \partial_0 (\bar{q}\gamma^0\gamma_5\vec{\lambda}\cdot q\vec{\phi}) \right]. \tag{A2}$$

We use this H_s in the derivation of the potential to follow where we separate off a vertex function V in the Fock-space Hamiltonian for $BM \leftrightarrow B_0'$:

$$V_{0i}(\mathbf{k}) = B_0'^{\dagger} \langle B_0' | \hat{H}_s | \alpha \rangle B_0, \tag{A3}$$

$$H_s = \sum_i \int d^3k \left[V_{0i}(\mathbf{k}) a_i(\mathbf{k}) + V_{0i}^{\dagger}(\mathbf{k}) a_i^{\dagger}(\mathbf{k}) \right]. \tag{A4}$$

APPENDIX B: $BM \leftrightarrow \Lambda_{S01}(1405)$ POTENTIAL

The quark model configuration for the bare $\Lambda_{S01}(1405)$ is one u, d, and s quark in an SU(3) flavor singlet, with one $1p_{1/2}$ quark and two $1s$ quarks. The transition $BM \to \Lambda_{S01}$ thus has one quark absorbing a meson and being excited from the $1s$ to $1p_{1/2}$ state. The quark wave functions are

$$q_{1s}^M(\mathbf{r},t) = \frac{N_s}{\sqrt{4\pi}} \begin{pmatrix} j_0(\omega_s r) \\ i\vec{\sigma}\cdot\hat{r}\, j_1(\omega_s r) \end{pmatrix} \chi_{\frac{1}{2}}^M e^{-i\omega_s t}\, \theta(R-r), \tag{B1}$$

$$q_{1p_{\frac{1}{2}}}^M(\mathbf{r},t) = \frac{N_{p1}}{\sqrt{4\pi}} \begin{pmatrix} -\vec{\sigma}\cdot\hat{r}\, j_1(\omega_{p1} r) \\ i j_0(\omega_{p1} r) \end{pmatrix} \times \chi_{\frac{1}{2}}^M e^{-i\omega_{p1} t}\, \theta(R-r), \tag{B2}$$

$$N_{s,p1}^2 = \frac{1}{2j_0^2(\omega_{s,p}R)R^3} \frac{\omega_{s,p}R}{\omega_{s,p} \mp 1}. \tag{B3}$$

Here χ is the spin-flavor wave function of the quark, j_0 and j_1 are spherical Bessel functions, $(\omega_s, \omega_{p1}) \approx (2.04/R, 3.81/R)$ are the energies of $1s$ and $1p_{1/2}$ states, and the N's are normalization constants [51]. The $BM \leftrightarrow \Lambda_{S01}(1405)$ vertex function needed in the Fock-space Hamiltonian H_s (A4) and the form factor for the Hamiltonian are accordingly

$$V_{0i}^{(S01)}(\mathbf{k}) = \Lambda_{1/2}^{\dagger}\, v_{\Lambda_{S01}\alpha}(\mathbf{k})\, B_0, \tag{B4}$$

$$v_{\Lambda_{S01}\alpha}(\mathbf{k}) = \langle \Lambda_{S01} | H_s | \alpha \rangle \tag{B5}$$

$$= \frac{-1}{2f} \frac{{}^{\mathrm{sf}}\langle \Lambda_{S01} | \lambda_i | B \rangle^{\mathrm{sf}}}{\sqrt{(2\pi)^3 2\omega_k}} N_s N_{p1} \left\{ 2R^2 j_0(\omega_s R) j_0(\omega_{p1} R) j_0(kR) + (\omega_k + \omega_s - \omega_{p1}) \int_0^R dr\, r^2 \left[j_0(\omega_s r) j_0(\omega_{p1} r) + j_1(\omega_s r) j_1(\omega_{p1} r) \right] j_0(kr) \right\}. \tag{B6}$$

The spin-flavor matrix element ${}^{\rm sf}\langle\Lambda_{S01}|\lambda_i|B\rangle^{\rm sf}$ is evaluated with the Wigner-Eckart theorem:

$$ {}^{\rm sf}\langle\Lambda_{S01}|\lambda_i|B\rangle^{\rm sf} = \lambda^{\Lambda}_{\alpha}\langle I_B i_B; I_M i_M | I_B I_M; 00\rangle, \tag{B7}$$

where the bracket on the right-hand side is a Clebsch-Gordan coefficient. The coupling constants $\lambda^{\Lambda}_{\alpha}$ are calculated using the SU(6) quark wave function [16,29] and are listed in Table II. The potential $v^{(S01)}(\mathbf{k}',\mu';\mathbf{k},\mu)$ corresponds to meson-baryon scattering through an intermediate Λ_{S01} state, Fig. 2:

$$ v^{(S01)}_{\beta\alpha} = \langle\beta|H_s|\Lambda_{S01}\rangle \frac{1}{E - M_{S01}} \langle\Lambda_{S01}|H_s|\alpha\rangle \tag{B8}$$

$$ = \frac{\delta_{\mu\mu'}\lambda^{\Lambda}_{\beta}\lambda^{\Lambda}_{\alpha}\langle I_{B'} i_{B'}; I_{M'} i_{M'} | I_{B'} I_{M'}; 00\rangle}{E - M_{S01}} \frac{\langle I_B i_B; I_M i_M | I_B I_M; 00\rangle}{64 f^2 \pi^3} \frac{u_{\Lambda_{S01}\beta}(k) u_{\Lambda_{S01}\alpha}(k)}{\sqrt{\omega_{k'}\omega_k}}. \tag{B9}$$

The partial wave matrix projection of this potential via (22) yields (35).

APPENDIX C: $BM \leftrightarrow \Lambda_{D03}(1520)$ POTENTIAL

The $\Lambda_{D03}(1520)$ has one u, d, and s quark in an SU(3) singlet with total spin 3/2 and wave function $1s^2\,1p_{3/2}$. The $\bar{K}N \to \Lambda_{D03}$ transition thus has one quark absorbing the antikaon and changing from $1s$ to the $1p_{3/2}$ (flavor may also change). The vertex function for the Foch-space Hamiltonian (A4) and the $1p_{3/2}$ quark wave function are

$$ V^{(D03)}_{0i}(\mathbf{k}) = \Lambda^{\dagger}_{3/2} \int d^3x e^{i\mathbf{k}\cdot\mathbf{r}} \frac{{}^{\rm sf}\langle\Lambda_{D03}|\delta_s \bar{q}_p \gamma_5 \lambda_i q_s + (\omega_s + \omega_k - \omega_{p3}) \bar{q}_p \gamma^0 \gamma_5 \lambda_i q_s | B\rangle^{\rm sf}}{-2fi\sqrt{(2\pi)^3 2\omega_k}} B_0, \tag{C1}$$

$$ q^M_{1p_{3/2}}(\mathbf{r},t) = N_{p3} \begin{pmatrix} j_1(\omega_{p3} r) \\ i j_2(\omega_{p3} r)(\boldsymbol{\sigma}\cdot\hat{r}) \end{pmatrix} \theta(R-r) e^{-i\omega_{p3} t} \mathcal{Y}^M_{1\frac{3}{2}}(\theta,\phi). \tag{C2}$$

Here $\mathcal{Y}^M_{lj}$ is the spin-angle function, N_{p3} is the $1p_{3/2}$ normalization constant [51], and $\omega_{p3} \approx 3.20/R$ is the energy level of the $1p_{3/2}$ state. We express the spin-angle function in terms of spherical harmonics and Pauli spinors, and substitute $|\Lambda_{D03}\rangle^{\rm sf} = \sum_m \langle 1m; \frac{1}{2}M - m | 1\frac{1}{2}; \frac{3}{2}M\rangle Y_{1m} |\Lambda_{S01}\rangle^{\rm sf}$ for the Λ_{D03} spin-flavor wave function (the same as Λ_{S01}) to obtain

$$ {}^{\rm sf}\langle\Lambda_{S01}(\mu-m)|\lambda_i\sigma_q|B(\nu)\rangle^{\rm sf} = -\sqrt{3}\,\lambda^{\Lambda}_{\alpha}\langle\tfrac{1}{2}\nu; 1q | \tfrac{1}{2}1; \tfrac{1}{2}\mu - m\rangle \langle I_B i_B; I_M i_M | I_B I_M; 00\rangle, \tag{C3}$$

$$ \begin{aligned} v_{\Lambda_{D03}\alpha}(\mu,\nu) = &-\frac{1}{2f}\frac{1}{\sqrt{3}} \frac{4\pi N_s N_{p3}}{\sqrt{(2\pi)^3 2\omega_k}} \sum_{mq}\sum_{LM} i^L (-1)^q \langle 1m; \tfrac{1}{2}\mu - m | 1\tfrac{1}{2}; \tfrac{3}{2}\mu\rangle Y^*_{LM}(\hat{k}) \\ &\times {}^{\rm sf}\langle\Lambda_{S01}(\mu-m)|\lambda_i\sigma_q|B(\nu)\rangle^{\rm sf} \int d^3x Y_{1-q}(\hat{r}) Y^*_{1m}(\hat{r}) Y_{LM}(\hat{r}) j_L(kr) \\ &\times \{\delta_s [j_1(\omega_s r) j_1(\omega_{p3} r) + j_0(\omega_s r) j_2(\omega_{p3} r)] \\ &\quad + \theta_v(\omega_s + \omega_k - \omega_{p3}) [j_1(\omega_s r) j_1(\omega_{p3} r) - j_0(\omega_s r) j_2(\omega_{p3} r)]\} \end{aligned} \tag{C4}$$

$$ \begin{aligned} = &\frac{1}{4\pi f\sqrt{3\omega_k}} \sum_{LM}\sum_{mq} (-1)^m i^L \sqrt{2L+1}\, Y^*_{LM}(\hat{k}) u^{(L)}_{\Lambda_{D03}\alpha}(k) \langle L0; 10 | L1; 10\rangle \\ &\times {}^{\rm sf}\langle\Lambda_{S01}(\mu-m)|\lambda_i\sigma_q|B(\nu)\rangle^{\rm sf} \langle 1m; \tfrac{1}{2}\mu - m | 1\tfrac{1}{2}; \tfrac{3}{2}\mu\rangle \langle LM; 1-m | L1; 1q\rangle, \end{aligned} \tag{C5}$$

$$ \begin{aligned} u^{(L)}_{\Lambda_{D03}\alpha}(k) = -N_s N_{p3} \Big[&2R^2 j_0(\omega_s R) j_1(\omega_{p3} R) j_L(kR) \\ &+ (\omega_s + \omega_k - \omega_{p3}) \int_0^R dr\, r^2 j_L(kr) [j_1(\omega_s r) j_1(\omega_{p3} r) - j_0(\omega_s r) j_2(\omega_{p3} r)] \Big]. \end{aligned} \tag{C6}$$

The coupling constants $\lambda^{\Lambda}_{\alpha}$ are the same as in the $BM \leftrightarrow \Lambda_{S01}$ case (Table II), and after lengthy algebraic manipulation of the Clebsch-Gordan coefficients and $6j$ symbols, we obtain the vertex function

$$
\begin{aligned}
v_{\Lambda_{D03}\alpha}(\mathbf{k};\mu,\nu) &= \frac{\lambda_\alpha^\Lambda}{4\pi f\sqrt{\omega_k}}\langle I_B i_B; I_M i_M | I_B I_M; 00\rangle \\
&\times \sum_{LM}\sum_{mq}(-1)^m i^L\sqrt{2L+1}Y^*_{LM}(\hat{k})\langle L0;10|L1;10\rangle u^L_{\Lambda_{D03}\alpha}(k) \\
&\times \langle 1m;\tfrac{1}{2}\mu - m|1\tfrac{1}{2};\tfrac{3}{2}\mu\rangle\langle LM;1{-}m|L1;1q\rangle\,\langle\tfrac{1}{2}\nu;1q|\tfrac{1}{2}1;\tfrac{1}{2}\mu - m\rangle \\
&= \frac{\lambda_\alpha^\Lambda u_{\Lambda_{D03}\alpha}(k)}{4\pi f\sqrt{\omega_k}}\langle I_B i_B; I_M i_M | I_B I_M; 00\rangle\langle\tfrac{1}{2}\nu;2\mu-\nu|\tfrac{1}{2}2;\tfrac{3}{2}\mu\rangle Y^*_{2(\mu-\nu)}(\hat{k}) \qquad \text{(C7)}
\end{aligned}
$$

The separable potential $v^{(D03)}$ corresponds to meson-baryon scattering through the intermediate Λ_{D03}, Fig. 2; i.e., using Λ_{D03} for B_0 in (18),

$$
\begin{aligned}
v^{(D03)}_{\beta\alpha}(\mathbf{k}',\mathbf{k}) &= \sum_\nu \langle\beta(\mu')|H_s|\Lambda_{D03}(\nu)\rangle\frac{1}{E - M_{D03}}\langle\Lambda_{D03}(\nu)|H_s|\alpha(\mu)\rangle \\
&= \frac{\lambda_\beta^\Lambda\lambda_\alpha^\Lambda u_{\Lambda_{D03}\beta}(k')u_{\Lambda_{D03}\alpha}(k)}{16\pi^2 f^2\sqrt{\omega_k\omega_{k'}}}\frac{\langle I_{B'}i_{B'};I_{M'}i_{M'}|I_{B'}I_{M'};00\rangle\,\langle I_B i_B;I_M i_M|I_B I_M;00\rangle}{E - M_{D03}} \\
&\times \sum_\nu Y^*_{2(\nu-\mu)}(\hat{k})Y_{2(\nu-\mu')}(\hat{k}')\langle\tfrac{1}{2}\mu;2\nu-mu|\tfrac{1}{2}2;\tfrac{3}{2}\nu\rangle\langle\tfrac{1}{2}\mu';2\nu-mu'|\tfrac{1}{2}2;\tfrac{3}{2}\nu\rangle. \qquad \text{(C8)}
\end{aligned}
$$

The partial wave projection of $v^{(D03)}$ involves extensive algebra and yields (34).

APPENDIX D: $BM \leftrightarrow \Sigma_{P13}(1385)$ POTENTIAL

The bare $\Sigma_{P13}(1385)$ is a single u, d, and s quarks in a **10** representation of SU(3), with all quarks in the $1s$ state. The transition $BM \to \Sigma_{P13}$ thus has one quark changing its flavor-spin state after absorbing a meson. The vertex function and form factor for the Foch-space Hamiltonian (A4) are accordingly

$$
\begin{aligned}
V^{(p)}_{0i}(\mathbf{k}) &= \Sigma^{0*\dagger}_{3/2}\,v_{\Sigma_{P13}\alpha}(\mathbf{k})\,B_0, \qquad \text{(D1)} \\
v_{\Sigma_{P13}\alpha}(\mathbf{k}) &= \Sigma^{0*\dagger}_{3/2}\,\langle\Sigma_{P13}|H_s|\alpha\rangle B_0 \qquad \text{(D2)} \\
&= \frac{1}{2f}\int\frac{d^3r}{\sqrt{(2\pi)^3 2\omega_k}}e^{i\mathbf{k}\cdot\mathbf{r}}\langle\Sigma_{P13}|i\delta_s\bar{q}_{1s}\gamma_5\lambda_i q_{1s} + i\theta_v\omega_k\bar{q}_{1s}\gamma^0\gamma_5\lambda_i q_{1s}|B\rangle \qquad \text{(D3)} \\
&= \frac{1}{2f}\frac{N_s^2}{4\pi}(-2)\int\frac{d^3r}{\sqrt{(2\pi)^3 2\omega_k}}e^{i\mathbf{k}\cdot\mathbf{r}}j_0(\omega_s r)j_1(\omega_s r)\delta_s{}^{\rm sf}\langle\Sigma_{P13}|\lambda_i\boldsymbol{\sigma}\cdot\hat{r}|B\rangle^{\rm sf} \qquad \text{(D4)} \\
&= \frac{1}{2f}\frac{N_s^2}{4\pi}\frac{-2}{\sqrt{(2\pi)^3 2\omega_k}}\int d^3r\,\delta_s 4\pi\sum_{LM}i^L j_L(kr)Y^*_{LM}(\hat{k})Y_{LM}(\hat{r}) \\
&\times j_0(\omega_s r)j_1(\omega_s r)\sum_q\sqrt{\frac{4\pi}{3}}Y^*_{1q}(\hat{r})^{\rm sf}\langle\Sigma_{P13}|\lambda_i\sigma_q|B\rangle^{\rm sf} \\
&= \frac{-iN_s^2R^2}{4f\sqrt{\pi^3\omega_k}}\sum_q Y^*_{1q}(\hat{k})j_0(\omega_s R)j_1(\omega_s R)j_1(kR)^{\rm sf}\langle\Sigma_{P13}|\lambda_i\sigma_q|B\rangle^{\rm sf}. \qquad \text{(D5)}
\end{aligned}
$$

To obtain the vertex function, we substitute (B1) for the $1s$ quark wave function, substitute the partial wave expansion of the plane wave, substitute the explicit form for $\boldsymbol{\sigma}\cdot\hat{r}$, and use the Wigner-Eckart theorem

$$
\boldsymbol{\sigma}\cdot\hat{r} = \sqrt{\frac{4\pi}{3}}\sum_q Y^*_{1q}(\hat{r})\sigma_q\,, \quad \sigma_{\pm1,0} = \mp\frac{1}{\sqrt{2}}(\sigma_x \pm \sigma_y),\ \sigma_z, \qquad \text{(D6)}
$$

$$
{}^{\rm sf}\langle\Sigma_{P13}(\mu)|\lambda_i\sigma_q|B(\nu)\rangle^{\rm sf} = \lambda^\Sigma_\alpha\langle\tfrac{1}{2}\nu;1q|;\tfrac{1}{2}1\tfrac{3}{2}\mu\rangle\langle I_B i_B;I_M i_M|I_B I_M;10\rangle \qquad \text{(D7)}
$$

$$
\begin{aligned}
v_{\Sigma_{P13}\alpha}(\mathbf{k};\mu,\nu) &= \frac{-i\lambda^\Sigma_\alpha N_s^2 R^2}{2\pi f\sqrt{3\omega_k}}\langle\tfrac{1}{2}\nu;1q|\tfrac{1}{2}1;\tfrac{3}{2}\mu\rangle\langle I_B i_B;I_M i_M|I_B I_M;10\rangle \\
&\times Y^*_{1(\mu-\nu)}(\hat{k})j_0(\omega_s R)j_1(\omega_s R)j_1(kR). \qquad \text{(D8)}
\end{aligned}
$$

The calculated coupling constants λ^Σ_α are given in Table II. The potential $v^{(P13)}(\mathbf{k}',\mu';\mathbf{k},\mu)$ is similar to $v^{(D03)}$, but now with an intermediate Σ_{P13} (Fig. 2):

$$v_{\beta\alpha}^{(P13)}(\mathbf{k}',\mathbf{k}) = \sum_{\nu}\langle\beta(\mu')|H_s|\Sigma_{P13}(\nu)\rangle\frac{1}{E-M_{P13}}\langle\Sigma_{P13}(\nu)|H_s|\alpha(\mu)\rangle \tag{D9}$$

$$= \frac{1}{12\pi^2 f^2\sqrt{\omega_{k'}\omega_k}}\frac{[N_s^2R^2 j_0(\omega_s R)j_1(\omega_s R)]^2}{E-M_{P13}} j_1(k'R)j_1(kR)\lambda_\beta^\Sigma\lambda_\alpha^\Sigma$$
$$\times\sum_{\nu} Y^*_{1(\nu-\mu)}(\hat{k})Y_{1(\nu-\mu')}(\hat{k}')\langle\tfrac{1}{2}\mu;1\nu-mu|\tfrac{1}{2}1;\tfrac{3}{2}\nu\rangle\langle\tfrac{1}{2}\mu';1\nu-mu'|\tfrac{1}{2}1;\tfrac{3}{2}\nu\rangle$$
$$\times\langle I_{B'}i_{B'};I_{M'}i_{M'}|I_{B'}I_{M'};10\rangle\langle I_B i_B;I_M i_M|I_B I_M;10\rangle. \tag{D10}$$

Its partial wave projection via (22) yields (35).

APPENDIX E: CONTACT POTENTIALS

The space-derivative part of the contact potential is

$$v_{\beta\alpha}^{(cs)}(\mathbf{k}',\mathbf{k}) = \frac{i^{\rm sf}\langle B'|\int d^3x\,\theta_v\bar{q}_{1s}f_{i'ij}\lambda_j(\mathbf{k}'+\mathbf{k})\cdot\boldsymbol{\gamma}e^{i(\mathbf{k}-\mathbf{k}')\cdot\mathbf{r}}q_{1s}|B\rangle^{\rm sf}}{8f^2(2\pi)^3\sqrt{\omega_k\omega_{k'}}} \tag{E1}$$

$$= \frac{iN_s^2}{4\pi}\int_0^R dr d\Omega_r\, r j_0(\omega_s r)j_1(\omega_s r)\,{}^{\rm sf}\langle B'|f_{i'ij}\lambda_j\boldsymbol{\sigma}|B\rangle^{\rm sf}$$
$$\times\frac{e^{-i\mathbf{k}'\cdot\mathbf{r}}(\mathbf{r}\times\mathbf{k})e^{i\mathbf{k}\cdot\mathbf{r}}+(\mathbf{r}\times\mathbf{k}')e^{-i\mathbf{k}'\cdot\mathbf{r}}e^{i\mathbf{k}\cdot\mathbf{r}}}{4(2\pi)^3 f^2\sqrt{\omega_k\omega_{k'}}}, \tag{E2}$$

where we have substituted for the quark wave functions q_{1s} and $q_{\bar{1}s}$. Since $\mathbf{r}\times\mathbf{k}$ and $\mathbf{r}\times\mathbf{k}'$ are the angular momentum operators acting on $e^{i\mathbf{k}\cdot\mathbf{r}}$ and $e^{i\mathbf{k}\cdot\mathbf{r}}$, substituting the partial wave expansions of the plane waves yields

$$v_{\beta\alpha}^{(cs)}(\mathbf{k}',\mathbf{k}) = \frac{iN_s^2\mathcal{A}}{f^2(2\pi)^2\sqrt{\omega_k\omega_{k'}}}\sum_{lmm'} Y^*_{lm}(\hat{k})Y_{lm'}(\hat{k}')\int_0^R dr\, j_0(\omega_s r)j_1(\omega_s r)j_l(kr)j_l(k'r), \tag{E3}$$

$$\mathcal{A} = {}^{\rm sf}\langle B'(\mu')|f_{i'ij}\lambda_j\boldsymbol{\sigma}|B(\mu)\rangle^{\rm sf}\int d\Omega_r Y^*_{lm'}\mathbf{L}Y_{lm}$$
$$= \sum_q(-1)^q\int d\Omega_r Y^*_{lm'}L_qY_{lm}\,{}^{\rm sf}\langle B'(\mu')|f_{i'ij}\lambda_j\sigma_{-q}|B(\mu)\rangle^{\rm sf}$$
$$= {}^f\langle B'||f_{i'ij}\lambda_j\boldsymbol{\sigma}||B\rangle f\sum_j(-1)^{\frac{1}{2}+j+l}\sqrt{l(l+1)(2l+1)}\begin{Bmatrix}\frac{1}{2}&\frac{1}{2}&1\\ l&l&j\end{Bmatrix}$$
$$\times\langle\tfrac{1}{2}\mu;lm|\tfrac{1}{2}l;jm'+\mu'\rangle\langle\tfrac{1}{2}\mu';lm'|\tfrac{1}{2}l;jm'+\mu'\rangle, \tag{E4}$$

where we have used the tensor notation for σ_{-q} and L_q as in (D6), the Wigner-Eckart theorem, and many manipulations. The calculated coupling constants $\lambda_{\beta\alpha}^{s,I}$ are given in Table II. After substituting all these relations back, we obtain

$$v_{\beta\alpha}^{(cs)}(\mathbf{k}',\mathbf{k}) = -N_s^2\sum_{I,jM,lmm'}\lambda_{\beta\alpha}^{s,I}\langle I_B i_B;I_M i_M|I_B I_M;I0\rangle\langle I_{B'}i_{B'};I_{M'}i_{M'}|I_{B'}I_{M'};I0\rangle$$
$$\times\langle\tfrac{1}{2}\mu;lm|\tfrac{1}{2}l;jM\rangle\langle\tfrac{1}{2}\mu';lm'|\tfrac{1}{2}l;jM\rangle Y^*_{lm}(\hat{k})Y_{lm'}(\hat{k}')\sqrt{6l(l+1)(2l+1)}$$
$$\times(-1)^{j+l+\frac{1}{2}}\int_0^R\frac{dr\,rj_0(\omega_s r)j_1(\omega_s r)j_l(kr)j_l(k'r)}{2f^2\pi^2\sqrt{\omega_k\omega_{k'}}}\begin{Bmatrix}\frac{1}{2}&\frac{1}{2}&1\\ l&l&j\end{Bmatrix}. \tag{E5}$$

The equations for $v^{(cs)}$ and $v^{(ct)}$ have the same form as Eqs. (2.8) and (2.9) in Ref. [17], but the coupling constants (spin-flavor matrix elements) in Table II are different. Finding the partial wave matrix elements of the potential $v^{(cs)}$ is more complicated. We start with the definition (19), apply the orthogonal relations of the spherical harmonics, the properties of the Clebsch-Gordan coefficients, and lengthy manipulations to obtain (43).

APPENDIX F: EXTENDED HAFTEL-TABAKIN TECHNIQUE

We give here our extension of the Haftel-Tabakin technique [28] for solving the Lippmann-Schwinger equation (23). For each channel γ the integrand in (23) contains an integrable singularity at the "on-shell" channel momentum

$k_{0\gamma} \equiv k_0$ defined in (17). To permit numerical integration this singularity is removed by subtracting a term from the integrand which leaves the integrand nonsingular [28], and then adding in the integral of the subtracted term:

$$\int_0^\infty dp\, \frac{p^2 V(k',p)T(p,k)}{E - E(p) + i\epsilon} = \int_0^\infty dp \left[\frac{p^2 V(k',p)T(p,k)}{E - E(p) + i\epsilon} - \frac{2\mu k_0^2 V(k',k_0)T(k_0,k)}{k_0^2 - p^2 + i\epsilon} \right] + 2\mu k_0^2 V(k',k_0)T(k_0,k) \int_0^\infty dp\, \frac{1}{k_0^2 - p^2 + i\epsilon} \tag{F1}$$

$$= \int_0^\infty dp \left[\frac{p^2 V(k',p)T(p,k)}{E - E(p)} - \frac{\pi\mu k_0^2 V(k',k_0)T(k_0,k)}{k_0^2 - p^2} \right] - \pi i \mu k_0 V(k',k_0)T(k_0,k), \tag{F2}$$

where the right-hand side of Eq. (F1) is evaluated analytically and where $\mu \equiv \mu_\gamma$ is the relativistic "reduced mass" for channel γ:

$$\mu_\gamma = \frac{1}{2} \left. \frac{dp^2}{dE_\gamma} \right|_{E_\gamma = E} = \frac{E_1(k_{0\gamma}) E_1(k_{0\gamma})}{E_1(k_{0\gamma}) + E_1(k_{0\gamma})}. \tag{F3}$$

We solve the integral equations (23) by approximating the integrals as sums over N Gaussian grid points $\{p_i | i = 1, N\}$ with weights $\{w_i | i = 1, N\}$:

$$T_{\beta\alpha}(k',k) = V_{\beta\alpha}(k',k) - \sum_\gamma 2i\mu_\gamma k_{0\gamma} V_{\beta\gamma}(k',k_{0\gamma}) T_{\gamma\alpha}(k_{0\gamma},k) + \frac{2}{\pi} \sum_{\gamma,i} \left[\frac{p_i^2 V_{\beta\gamma}(k',p_i) T_{\gamma\alpha}(p_i,k)}{E - E_\gamma(p_i)} - \frac{2\mu_\gamma k_{0\gamma}^2 V_{\beta\gamma}(k',k_{0\gamma}) T_{\gamma\alpha}(k_{0\gamma},k)}{k_{0\gamma}^2 - p_i^2} \right]. \tag{F4}$$

We convert (F4) to the set of linear equations

$$T_{n\beta,m\alpha} = V_{n\beta,m\alpha} + \sum_{\gamma=1}^{N_c} \sum_{i=1}^{N+1} V_{n\beta,i\gamma} G_{i\gamma} T_{i\gamma,m\alpha} \tag{F5}$$

by defining the supematrix elements for G, V, and T:

$$V_{n\beta,m\alpha} = \begin{cases} V_{\beta\alpha}(p_n,p_m) & (n = 1\,N,\ \ m = 1\,N), \\ V_{\beta\alpha}(k_{0\beta},p_m) & (n = N+1,\ m = 1\,N), \\ V_{\beta\alpha}(p_n,k_{0\alpha}) & (n = 1\,N,\ \ m = N+1), \\ V_{\beta\alpha}(k_{0\beta},k_{0\alpha}) & (n = N+1,\ m = N+1), \end{cases} \tag{F6}$$

$$G_{n\gamma} = \begin{cases} 2w_n p_n^2 / [\pi(E - E_\gamma(p_n)] & (n = 1\,N), \\ -2\mu_\gamma \sum_{i=1}^N [2w_i k_{0\gamma}^2 / \pi(k_{0\gamma}^2 - p_i^2)] - ik_{0\gamma} 2\mu_\gamma & (n = N+1). \end{cases} \tag{F7}$$

Here $T_{n\beta,m\alpha}$ are the $N_c^2(N+1)^2$ unknowns for N_c channels and N Gaussian grid points (the +1 arising from the on-shell point). The potential V is taken as the sum of the 5 terms in (18), $N_c = 5$ for the five independent isospin channels in (24), and we use 24 or 32 Gaussian grid points in each channel. We then solve the $N_c^2(N+1)^2$ coupled equations (F5) by rearranging the matrix equation

$$[T] = [V] + [VG][T] \tag{F8}$$

$$\Rightarrow \quad [1 - VG][T] = [V] \tag{F9}$$

$$\Rightarrow \quad [T] = [1 - VG]^{-1}[V]. \tag{F10}$$

Because the solution for T is numerically intensive, we have made a number of improvements to our former technique. First, while we previously determined the actual inverse $[1 - VG]^{-1}$ and evaluated (F10), we now solve (F9) for T using Gaussian elimination. This is $\sim$ 30% faster than matrix inversion. Next we obtain an even greater savings by utilizing the symmetry of the potential V and the diagonal nature of the Green's function G to reformulate (F9) as

$$[G^{-1} - V][GT] = [V]. \tag{F11}$$

Since $[G^{-1} - V]$ is symmetric, we solve a symmetric linear system of equations for $[GT]$—which is much faster than a general system. From this $[GT]$ we easily obtain the value of $[T]$ since $[G]$ is a diagonal and its inverse is quick to compute.

If there are some elements of G which vanish, the reformulation is a little more complicated. For example, we assume the last element of G vanishes while none of the others do (if it is not the last element, we can always rearrange columns and rows to make it last). The linear system is now

$$\begin{bmatrix} 1-vg & 0 \\ -v_r g & 1 \end{bmatrix} \begin{bmatrix} t & t_c \\ t_r & t_M \end{bmatrix} = \begin{bmatrix} v & v_c \\ v_r & v_M \end{bmatrix}. \quad \text{(F12)}$$

Here v is an $(M-1)\times(M-1)$ *symmetric* matrix, g is a $(M-1)\times(M-1)$ diagonal matrix, t is a $(M-1)\times(M-1)$ matrix, v_r and t_r are $(M-1)\times 1$ row matrices, v_c and t_c are $(M-1)\times 1$ column matrices, and v_M and t_M are the lower right-hand corner elements of V and T. We split (F12) into the equations

$$(1-vg)t = v, \quad \text{(F13)}$$

$$(1-vg)t_c = v_c, \quad \text{(F14)}$$

$$-v_r g t + t_r = v_r, \quad \text{(F15)}$$

$$-v_r g t_c + t_M = v_M, \quad \text{(F16)}$$

and solve for t and t_c with the *symmetric* matrix v (this is fast). We then solve for t_r and t_M if needed. If there are several elements in G which vanish, we follow the same procedure recursively until we are left with a symmetric system to solve. In practice, the direct lower triangular–upper triangular (LU) decomposition method took 1214 s on an IBM RS/6000 Model-530, while the method using symmetry took 493 s.

[1] A. Chodos, R. L. Jaffe, K. Johnson, C. B. Thorn, and V. F. Weisskopf, Phys. Rev. D **9**, 3471 (1974).

[2] H. Pagels, Phys. Rep. **16**, 219 (1975).

[3] A. Chodos and C.B. Thorn, Phys. Rev. D **12**, 2733 (1975).

[4] G.E. Brown and M. Rho, Phys. Lett. **82B**, 177 (1979); **84B**, 383 (1979).

[5] R.L. Jaffe, in *Proceedings of the 7th International School of Subnuclear Physics*, Erice, 1979, edited by A. Zichichi (Plenum, New York, 1982), p. 99.

[6] G.A. Miller, A.W. Thomas, and S. Théberge, Phys. Lett. **91B**, 192 (1980).

[7] S. Théberge, A.W. Thomas, and G.A. Miller, Phys. Rev. D **22**, 2838 (1980).

[8] G.A. Miller, A.W. Thomas, and S. Théberge, Comments Nucl. Part. Phys. **10**, 101 (1981).

[9] A.W. Thomas, S. Théberge, and G.A. Miller, Phys. Rev. D **24**, 216 (1981).

[10] A.W. Thomas, J. Phys. G **7**, L283 (1981).

[11] S. Théberge, G.A. Miller, and A.W. Thomas, Can. J. Phys. **60**, 59 (1982).

[12] S. Théberge and A.W. Thomas, Nucl. Phys. **A393**, 252 (1983).

[13] A.W. Thomas, in *Advances in Nuclear Physics*, edited by J. Negele and E. Vogt (Plenum, New York, 1984), Vol. 13, p. 1.

[14] E.A. Veit, B.K. Jennings, and A.W. Thomas, Phys. Rev. D **33**, 1859 (1986).

[15] E.D. Cooper, B.K. Jennings, P.A.M. Guichon, and A.W. Thomas, Nucl. Phys. **A469**, 717 (1987).

[16] E.A. Veit, B.K. Jennings, A.W. Thomas, and R.C. Barrett, Phys. Rev. D **31**, 1033 (1985).

[17] E.A. Veit, A.W. Thomas, and B.K. Jennings, Phys. Rev. D **31**, 2242 (1985).

[18] E.A. Veit, B.K. Jennings, R.C. Barrett, and A.W. Thomas, Phys. Lett. **137B**, 415 (1984).

[19] P.J. Fink, G. He, R.H. Landau, and J.W. Schnick, Phys. Rev. C **41**, 2720 (1990).

[20] J.D. Davies, G.J. Pyle, G.T.A. Squier, C.J. Batty, S.F. Biagi, S.D. Hoath, P. Sharman, and A.S. Clough, Phys. Lett. **83B**, 55 (1979).

[21] M. Izycki, G. Backenstoss, L. Tauscher, P. Blum, R. Guigas, N. Hassler, H. Koch, H. Poth, K. Fransson, A. Nilsson, P. Pavlopoulos, and K. Zioutas, Z. Phys. A **297**, 11 (1980).

[22] P.M. Bird, A.S. Clough, and K.R. Parker, Nucl. Phys. **A404**, 482 (1983).

[23] J. Schnick and R.H. Landau, Phys. Rev. Lett. **58**, 1719 (1987); J.W. Schnick, Ph.D. thesis, Oregon State University, 1988.

[24] K. Tanaka and A. Suzuki, Phys. Rev. C **45**, 2068 (1992).

[25] K.S. Kumar and Y. Nogami, Phys. Rev. D **21**, 1834 (1980).

[26] J. Ciborowski, J. Gwizdz, D. Kielczewska, R.J. Nowak, E. Rondio, J.A. Zakrzewski, M. Goossens, G. Wilquet, N.H. Bedford, D. Evans, G.P. Fleming, Y.A. Hamam, J.V. Major, J.H. Bartley, D.H. Davis, D.J. Miller, D.N. Tovee, and T. Tymieniecka, J. Phys. G **8**, 13 (1982).

[27] R.H. Landau, *Quantum Mechanics II* (Wiley, New York, 1990).

[28] M.I. Haftel and F. Tabakin, Nucl. Phys. **158**, 1 (1970).

[29] W.M. Gibson and B.R. Pollard, *Symmetry Principles in Elementary Particle Physics* (Cambridge University Press, Cambridge, England, 1976).

[30] M.B. Watson, M. Ferro-Luzz, and R.D. Tripp, Phys. Rev. **131**, 2248 (1963).

[31] M. Sakitt, T.B. Day, R.G. Glasser, N. Seeman, J. Friedman, W.E. Humphrey, and R.R. Ross, Phys. Rev. **139**, 719 (1965).

[32] J.K. Kim, Phys. Rev. Lett. **14**, 29 (1965); **19**, 1074 (1967).

[33] W. Kittel, G. Otter, and I. Wacek, Phys. Lett. **21**, 349 (1966).

[34] T.S. Mast, M. Alston-Garnjost, R.O. Bangerter, A.S. Barbaro-Galtieri, F.T. Solmitz, and R.D. Tripp, Phys. Rev. D **11**, 3078 (1975); **14**, 13 (1976).

[35] R.O. Bangerter, M. Alston-Garnjost, A. Barbaro-Galtieri, T.S. Mast, F.T. Solmitz, and R.D. Tripp, Phys. Rev. **23**, 1484 (1981).

[36] D. Evans, J.V. Major, E. Rondio, J.A. Zakrzewski, J.E. Conboy, D.J. Miller, and T. Tymieniecka, J. Phys. G **9**, 885 (1983).

[37] R.J. Hemingway, Nucl. Phys. **B253**, 742 (1985).

[38] R.H. Dalitz and A. Deloff, J. Phys. G **17**, 289 (1991).

[39] M. Aguilar-Benitez and J. Salicio, An. Fis. A **77**, 144 (1981).

[40] W.E. Humphrey and R.R. Ross, Phys. Rev. **127**, 1305 (1962).

[41] D.N. Tovee, D.H. Davis, and J. Simonovic, Nucl. Phys. **B33**, 493 (1971).

[42] R.J. Nowak, J. Armstrong, and D.H. Davis, Nucl. Phys. **B139**, 61 (1978).

[43] M. Goossens, G. Wilquet, J.L. Armstrong, and J.H. Bartley, in *Low and Intermediate Energy Kaon-Nucleon Physics*, edited by E. Ferrari and G. Violini (Reidel, Dordrecht, 1980).

[44] M. Alberg, E. M. Henley, and L. Wilets, Ann. Phys. (N.Y.) **96**, 43 (1976).

[45] R.H. Landau and B. Cheng, Phys. Rev. C **33**, 734 (1986).
[46] Y. Umino and F. Myhrer, Phys. Rev. D **39**, 3391 (1989).
[47] D.B. Leinweber, Ann. Phys. (N.Y.) **198**, 203 (1990).
[48] Particle Data Group, Phys. Lett. B **239**, 1 (1990).
[49] D. Gill (private communication).
[50] R.H. Landau, Phys. Rev. C **27**, 2191 (1983).
[51] A.J.G. Hey, in *Proceedings of the 8th International Seminar on Theoretical Physics*, Salamanca, Spain, edited by J.A. de Azcárraga (Springer-Verlag, Berlin, 1978), Vol. 77, p. 155.
[52] M. Guidry, *Gauge Field Theories* (Wiley, New York, 1991).